

Detailed Modelling for Photocurrent Spectra of $\text{In}_{0.91}\text{Ga}_{0.09}\text{N}/\text{In}_{0.4}\text{Ga}_{0.6}\text{N}$ Disk-in-Wire Photodiode Operating in $1.3\ \mu\text{m} - 1.55\ \mu\text{m}$

Fu-Chen Hsiao,^{*,†} Arnab Hazari,[‡] Pallab Bhattacharya,[‡] Yia-Chung Chang,[¶] and
 John Dallesasse[†]

[†]*Department of Electrical and Computer Engineering, University of Illinois at
 Urbana-Champaign, Urbana, Illinois 61801, United States*

[‡]*Department of Electrical Engineering and Computer Science, University of Michigan,
 1301 Beal Avenue, Ann Arbor, Michigan 48109-2122, United States*

[¶]*Research Center for Applied Sciences, Academia Sinica, Taipei 11529, Taiwan*

E-mail: fhsiao3@illinois.edu

Abstract

This work reports detailed modelling of photocurrent spectra generated by an $\text{In}_{0.91}\text{Ga}_{0.09}\text{N}/\text{In}_{0.4}\text{Ga}_{0.6}\text{N}$ disk-in-wire photodiode. The strain distribution is calculated by valence-force-field (VFF) model, while realistic band structure of InN/InGa_N heterostructure is incorporated by eight-band effective bond-orbital model (EBOM) with spin-orbit coupling is neglected. The electrostatic potential is obtained from self-consistent calculation based on effective-mass model with non-equilibrium Green's function method (NEGF), and served as input for the multi-band transfer-matrix-method (TMM) to calculate the tunnelling coefficients of optical-pumped carrier in absorbing region. The photocurrent spectra contributed by both single-photon absorption (SPA)

and two-photon absorption (TPA) are calculated, which the photon density-of-state (DOS) at the nanowire region are included by applying rigorous coupled-wave analysis (RCWA). The calculated photocurrent spectra is in good agreement with experimental data, while the photon absorption process at each peaks are identified and investigated.

Introduction

Integration of III-V devices on silicon is a well-known technique for overcoming low efficiency of photon-absorbing/emitting process in Si-based photodetector/laser.¹⁻³ The direct epitaxial growth of III-V materials and heterostructure on silicon appears as the most straightforward method to achieve III-V on silicon integration.⁴⁻⁶ However, due to high density of threading dislocations, mismatch of thermal expansion coefficients, and formation of antiphase domains, the direct epitaxial growth method encounters many problems that have not been properly solved.

Instead of planar structure, growing nanowires structure consist of III-nitride (III-N) semiconductor in WZ phases provides a very different scope to deal with the problem on III-V/Si integration.⁷⁻⁹ Due to efficient lateral-strain relaxation at the nanowire-silicon interface, nanowires heterostructure shows efficient reduction of polarization field,¹⁰ and further achieve smaller radiative recombination time than the system with quantum well (QW) structure.⁷ From the simulation perspective, the modelling for high-indium content III-N based device in WZ phase presents multiple challenges. The ambiguity introduced by the ordering of the operators may lead to spurious solutions in $k \cdot p$ model,^{12,13} especially in the large wavevector region for high-indium content devices due to the uncertainty of band parameters in InN. This indicates that a band structure model which is capable of producing accurate band structure in the full BZ is needed. Besides that, hexagonal structures present much less symmetry (C_{3v}) than the one in cubic phase (T_d), which introduces multiple extra fitting parameters in the band structure model and lead to wrong effective-mass. As a result, a semi-empirical model which is capable of producing full band structure, while the effective masses

are fixed at the desired values (i.e. experimental value) is required. Furthermore, since the optical transition is not necessary to happen near the BZ center for high-indium content devices, the optical matrix elements which includes wavevector dependence are required as well. Recently, a novel monolithic optical interconnect on a (001)Si substrate using InGaN disk-in-wire array, which consist of edge emitting diode laser and guided wave photodiode, has been demonstrated experimentally.¹¹ To the best of author's knowledge, due to the complexity of geometry, ultra-high indium content active region, and the requirement of realistic band structure within a large portion of 1st Brillouin zone (BZ), a systematic study of the photon absorption process as well as the carrier tunnelling behaviours is not available.

In this work, we provide a theoretical analysis for the photocurrent spectra of high-indium content InN/InGaN disk-in-wire photodiode with guided wave structure base on the eight-band EBOM.¹⁴⁻¹⁶ The theoretical model covers the strain distribution, polarization field effect (piezoelectric and spontaneous), and realistic band structure of InN/InGaN with semi-infinite boundary condition for modelling quantum carrier transport. The photon DOS corresponds to the resonance states in the photodiode is incorporated in the model by calculating the complex-band structure of InN/InGaN waveguide structure using RCWA,¹⁷ and fitted with Lorentzian functions by cut-off energies and resonance bandwidth. The simulation provides detailed descriptions on the corresponding optical transition process for each peaks on the photocurrent spectra. The comparison of calculated photocurrent spectra and the measured data are presented as well.

Electronic States of Single $\text{In}_x\text{Ga}_{1-x}\text{N}$ Disk-in-Wire Structure

We first examine the electronic state in a single $\text{In}_x\text{Ga}_{1-x}\text{N}$ disk-in-wire structure. The model presented in this section will be used to determine the geometric parameters and indium model fraction in disk region by fitting the calculated ground-state transition energy with the

dominant peak in the experimental photoluminescence (PL) measurement. The electronic states of quantum disk (QD) depend significantly on the strain distribution in III-N system. The strain field influences the electronic states of a QD in two phases: direct by strain-induced deformation potential and indirect by strain-induced piezoelectric polarizations. In addition to piezoelectric polarization, due to high electronegativity of nitrogen atom, the spontaneous (pyroelectric) polarization presents in [0001] direction of WZ crystals. Since the VFF model can give a strain tensor on the atomistic level, avoid potential failure at the interface, and retain the correct point symmetry of the system, the VFF model is chosen in favor of the continuum mechanical model in this work, which is described in Refs. 18–20. All the parameters for III-N materials used in VFF model are adopted from Ref. 21, where the linear interpolation has been used for $\text{In}_x\text{Ga}_{1-x}\text{N}$ alloys. Given the local strain tensor, the strain-induced deformation potential is then incorporated in the EBOM Hamiltonian according to Bir-Pikus theory.²²

Since the lateral size of the disk region is fairly large (> 20 nm), the quantum confinement effect is dominant in [0001] direction. As a result, an eight-band EBOM for WZ crystal¹⁶ is applied in growth direction to calculate electronic state in a QW to obtain the main features of the energy spectrum. All the EBOM parameters used in this work are adopted from Ref 16. Given the QW subband structure in lateral wavevectors (\mathbf{k}_{\parallel}), the kinetic energy and confinement effect corresponds to the potential fluctuation in lateral direction are described by effective-mass model (EFM) with the values of the effective-masses are adopted from calculated QW subband structure. Base on the calculation scheme mentioned above, the Hamiltonian of the whole system is decomposed into two parts:

$$H_{tot} = H^{(0)} + H^{(1)}. \quad (1)$$

In Eq. (1), the zero-order Hamiltonian includes the kinetic energy and confinement effect in [0001] direction, which the potential in each layer are taken as the average of corresponding xy -plane. The first-order term accounts to kinetic energies and potential confinement effect

in lateral direction. The zero-order Hamiltonian is constructed in eight-band effective bond-orbital basis, while the first-order Hamiltonian is constructed by using EFM. An appropriate EBOM is chosen for each participating III-N material in the QW. The interactions between any two bond-orbitals located in the same material are taken to be the same as those for the bulk. The interaction parameters between two bond-orbitals located in two different materials (i.e. the interaction parameters across the heterojunction) are obtained as the average of the corresponding matrix elements in the two participating bulk materials. Once the interactions among all bond-orbitals in the QW are defined, one may proceed in several ways to calculate the electronic structures. Due to the simplicity of the structure considered here, the direct diagonalization method adopted in our case.

Now the goal turns to building up the lateral associated Hamiltonian, $H^{(1)} = T_{xy} + \Delta V$, under effective-mass approximation. The basis functions are taken as direct product of envelope-functions associated r, ϕ and z directions, $|n, m, \nu\rangle$, where n denotes the subband index in z -direction, m denotes the order of the Bessel function, and ν are the index corresponds to the zeros of Bessel function. The envelope-function in z -direction are obtained from the EBOM Hamiltonian, and only the envelope-function corresponds to selected subband are included here to reduce the computation time, namely, only few subband with energies close to band gap are considered. The matrix elements of the kinetic energy component for $H^{(1)}$ can be written as

$$\begin{aligned} \langle n', m', \nu' | T_{xy} | n, m, \nu \rangle &= \sum_k \langle n', m', \nu' | k \rangle \langle k | T_{xy} | k \rangle \langle k | n, m, \nu \rangle \\ &= \sum_k \langle m', \nu'; k | \otimes \langle n'; k | T_{xy} | n; k \rangle \otimes | m, \nu; k \rangle. \end{aligned} \quad (2)$$

The expectation values of the lateral kinetic energies in $|n\rangle$ basis is simply determined by the lateral band structure from EBOM:

$$\langle n'; k | T_{xy} | n; k \rangle = \delta_{nn'} [E_n^{ebom}(k) - E_n^{ebom}(0)], \quad (3)$$

where $E_n^{ebom}(k)$ is the EBOM energy at lateral momentum k corresponds to subband n . The vector $|m, \nu; k\rangle$ is the Fourier transform of the lateral basis function:

$$|m, \nu; k\rangle = \mathcal{F}[R_{m,\nu}(\rho)\Phi(\phi)] = \mathcal{F}\left[\frac{1}{\sqrt{N_\nu^m}} J_m(\alpha_\nu^m \rho) \frac{1}{\sqrt{2}} e^{im\phi}\right], \quad (4)$$

The constant N_ν^m is normalization factor of radial basis function, which is determined by vanishing boundary condition radius, r_0 , and zeros of m -order Bessel function, x_ν^m :

$$N_\nu^m = \frac{r_0^2}{2} J_{m+1}^2(x_\nu^m). \quad (5)$$

For more compact expression, we use $C_\nu^m = 1/\sqrt{2\pi N_\nu^m}$ for the normalization factor in the following derivation. The Fourier basis function can be expanded in cylindrical basis according to Jacobi-Anger identity as

$$e^{-i\mathbf{k}\cdot\mathbf{r}} = \sum_{m,\nu} (-1)^{\nu+m} i^m 2\sqrt{\pi} \alpha_\nu^m \frac{J_{|m|}(kr_0)}{k^2 - (\alpha_\nu^m)^2} e^{im\phi_k} C_\nu^m J_m(\alpha_\nu^m \rho) e^{-im\phi}. \quad (6)$$

The Fourier transform of the cylindrical basis function then is obtained as

$$\sum_{p,q} D_q^p(\mathbf{k}) \int_0^{r_0} \int_0^{2\pi} C_q^p J_p(\alpha_q^p \rho) e^{-ip\phi} C_\nu^m J_m(\alpha_\nu^m \rho) e^{im\phi} \rho d\rho d\phi, \quad (7)$$

where

$$D_\nu^m(\mathbf{k}) = \frac{1}{2\pi} (-1)^{\nu+m} i^m 2\sqrt{\pi} \alpha_\nu^m \frac{J_{|m|}(kr_0)}{k^2 - (\alpha_\nu^m)^2} e^{im\phi_k}. \quad (8)$$

Notice that, $\mathbf{k} = (k, \phi_k)$ is now the wavevector variable corresponds to Fourier transform.

Applying the orthogonality relation of the cylindrical basis function, one obtain

$$\mathcal{F}[R_{m,\nu}(\rho)\Phi(\phi)](\mathbf{k}) = \sum_{p,q} D_q^p(\mathbf{k}) \delta_{m,p} \delta_{\nu,q} = D_\nu^m(\mathbf{k}). \quad (9)$$

The full expression of matrix element associate to kinetic energy, Eq. (3), is then obtained

as

$$\begin{aligned}
\langle n', m', \nu' | T_{xy} | n, m, \nu \rangle &= \sum_k \delta_{nn'} [E_n^{ebom}(k) - E_n^{ebom}(0)] \{ [D_{\nu'}^{m'}(k)]^* \times [D_{\nu}^m(k)] \} \\
&= \delta_{nn'} \int_0^\infty \int_0^{2\pi} [E_n^{ebom}(k, \phi_k) - E_n^{ebom}(0)] I_{\nu'\nu}^{m'm} \frac{J_{|m'|}(kr_0) J_{|m|}(kr_0)}{[k^2 - (\alpha_{\nu'}^{m'})^2][k^2 - (\alpha_{\nu}^m)^2]} e^{i(m-m')\phi_k} k dk d\phi_k
\end{aligned} \tag{10}$$

where

$$I_{\nu'\nu}^{m'm} = \frac{1}{\pi} (-1)^{\nu'+\nu+m} (i)^{m'+m} \alpha_{\nu'}^{m'} \alpha_{\nu}^m. \tag{11}$$

For the potential part, the matrix elements can be written as

$$\begin{aligned}
\langle n', m', \nu' | \Delta V | n, m, \nu \rangle &= \sum_{\mathbf{r}} \langle n', m', \nu' | \mathbf{r} \rangle \langle \mathbf{r} | \Delta V | \mathbf{r} \rangle \langle \mathbf{r} | n, m, \nu \rangle \\
&= \sum_{\mathbf{r}} \Delta V(\rho, \phi, z) \langle n' m', \nu'; \mathbf{r} | n, m, \nu; \mathbf{r} \rangle.
\end{aligned} \tag{12}$$

The vector $|n, m, \nu; \mathbf{r}\rangle$ is the direct product of the envelope-function in z-direction and the lateral basis functions:

$$|n, m, \nu; \mathbf{r}\rangle = |n; \mathbf{r}\rangle \otimes |m, \nu; \mathbf{r}\rangle = f_n(z) C_{\nu}^m J_m(\alpha_{\nu} \rho) e^{im\phi}. \tag{13}$$

Eq. (12) hence becomes

$$\begin{aligned}
\langle n', m', \nu' | \Delta V | n, m, \nu \rangle &= \int f_{n'}^*(z) f_n(z) \Delta V(z) dz \\
&\times \int_0^{2\pi} \int_0^{r_0} C_{\nu'}^{m'} C_{\nu}^m J_{m'}(\alpha_{\nu'}^m \rho) J_m(\alpha_{\nu}^m \rho) \Delta V(\rho, \phi) \rho d\rho d\phi.
\end{aligned} \tag{14}$$

In this manner, the electronic states in $\text{In}_x\text{Ga}_{1-x}\text{N}$ disk-in-wire can be solved efficiently in the subspace of the full Hamiltonian defined by the selected subband states obtained from EBOM.

Leaking Rate in Quantum Well System: Multi-Band Transfer Matrix Method

In order to study photocurrent spectra, the carrier leaking rate considering the full device epitaxial structure is required. There are multiple different theoretical methods for evaluating the carrier tunnelling rate, including the phase-shift method,²³ the complex-energy method,²⁴ and the stabilization method.^{25,26} The main drawback for both the phase-shift method and the complex-energy method is the requirement of wavefunctions. In contrast, the stabilization method requires only the eigenvalues of the system Hamiltonian as functions of an external parameters, which refer to the scaling factors. It can calculate the electron/hole leaking rate (or carrier lifetime) given the actual coupling strength between states, and the width of the generated DOS averaged by scaling parameter. However, it is impractical when considering device with complicated structure which possess multiple tunnelling channels. Besides that, the stabilization method can not really incorporate the continuum-to-continuum state transition. As a result, we adopt a method which is based on transfer-matrix-method (TMM) to calculate the reflection coefficient spectra of the InN/InGaN disk-in-wire photodiode, and further obtain the leaking rate of bound or quasi-bound state in the disk region. Again, the band structure information is incorporated via eight-band EBOM, while boundary conditions are applied at the contact region (or the boundary of the simulation domain) by linking the band structure in the device region to complex-band structure in plane-wave basis.

A numerically stable version of multi-band TMM base on EBOM for the devices composed of ZB semiconductor can be found in Ref 27, which can be easily extended into the system with WZ materials. The only difference is to considering an unit-cell containing two monolayers due to hexagonal crystal structure. For the EBOM with only nearest-neighbour interaction in WZ material system, the matrix inversion of Hamiltonian in planar orbital basis fails due to singularity. As a result, we calculate the inter-layer coupling explicitly

in the case of WZ crystal to avoid this issue. In our experience, instead of constructing an eigenvalue equation when calculating the complex-band structure and the corresponding eigenvectors at boundaries, it is numerically more stable to construct a generalized eigenvalue equation. The reflection coefficients which obtained from the TMM can be used as the leaking rate for the bound or quasi-bound state in the active region, which quantitatively describe the carriers in the active region tunnel through the barrier and further achieve contact. These values are utilized when calculating the photocurrent strength of InN/InGaN disk-in-wire photodiode.

The idea of using reflection coefficients to describe the leaking rate (or tunnelling rate) of carriers in the active region is rather simple. In the TMM model, the incident wave from the contact serves as the input of the calculation. Normally, we assign the magnitude of the incident wave to be one at certain available channel which determined from the complex-band structure. In this manner, the magnitude of reflected and transmitted can be easily calculated by comparing with the amplitude of assigned incident wave. If the system is composed of non-absorbing material, the sum of the transmission and reflection coefficient should be identical. In the other hand, if a finite absorption presents in the system, the incident wave is absorbed by the material which the amount is proportional to the magnitude of the wavefunction inside the bounding area. In this work, we artificially introduce a small absorption in the system, and a sharp peak appears in the reflection spectra due to the fact that the energy of incident wave matches the one of bound or quasi-bound state. The incident wave can be realized as a trigger state, which excites the bound state when its energy hits the resonant energies, and lead to a strong absorption due to relatively large magnitude of the bound state in the active region. As for the incident waves with energies which does not match any bound states or quasi-bound states, these incident waves bounce back with almost full magnitude and contribute relatively large reflection coefficients in the reflectance spectra. This method allows us to localize the energies of bound states (or quasi-bound state, depends on the ratio of wave function magnitude across the interface between

the barrier and active region.), at the same time, the actual wavefunction can be generated from the TMM. Notice that the artificial adsorption presents as a imaginary value of energy in the calculation, and introduce energy broadening in the energy spectra. This value is proportional to the carrier lifetime of the carrier in that particular state. As a result, the artificial imaginary part of the energy can not be larger than the actual energy broadening in the experimental spectra. As a demonstration of the idea, we shows the calculated leaking rate spectra of a InN/InGaN multi-QW structure for both the quasi-bound states and the non-resonance states as shown in Fig. (1). The first row shows the case when the selected energies are at resonance with quasi-bound states, while the second row shows the case when the selected energies are out of resonance.

Determination of Indium Mole Fraction at Disk Region

In this section, we perform the calculation of electronic state of single $\text{In}_x\text{Ga}_{1-x}\text{N}/\text{In}_{0.4}\text{Ga}_{0.6}\text{N}$ disk-in-wire structure, which is presented in Sec. (2), aim to determine the indium mole fraction at disk region by fitting with the energy of dominant PL peak. The detailed description of structure and measured PL data of the InN/InGaN disk-in-wire structure can be found in Ref 11. Notice that, the periodic boundary condition in the [0001] is applied in the VFF model to incorporate the multi-disks in single wire structure, while flexible boundary condition is adopted in xy -plane. As illustrated in Fig. (2), the geometric parameters of the considered structure are as follows. An $\text{In}_x\text{Ga}_{1-x}\text{N}$ disk, which the lateral diameter equals to 299.8 Å and height equals to 62.4 Å, embedded in a $\text{In}_{0.4}\text{Ga}_{0.6}\text{N}$ hexagonal prism supercell with side length equals to 300 Å and hight equals to 177.5 Å. The geometric parameters above serve as input geometry in VFF model and are obtained by examining the TEM-HAADF and EDS images in Ref 11. The best fit with the dominant PL peak measured at 13K occurs at 0.7485 eV (z -direction) +0.0075 (lateral direction) = 0.7560 eV with the indium composition inside the active region of disk is $\sim 91\%$.

The strain distribution corresponds to $\text{In}_{0.91}\text{Ga}_{0.09}\text{N}$ disk-in-wire structure in xy -plane and z -direction are shown in Fig. (3) and Fig. (4), respectively. Figure (5) shows the diagonal elements of the strain Hamiltonian along $[100]$, $[010]$, and $[001]$ directions. Here $V_{ss} = a_2(\epsilon_{xx} + \epsilon_{yy}) + a_1\epsilon_{zz}$, $V_{xx} = l_1\epsilon_{xx} + m_1\epsilon_{yy} + m_2\epsilon_{zz}$, $V_{yy} = m_1\epsilon_{xx} + l_1\epsilon_{yy} + m_2\epsilon_{zz}$, and $V_{zz} = m_3(\epsilon_{xx} + \epsilon_{yy}) + l_2\epsilon_{zz}$. We see that the hydrostatic strain is approximately uniform throughout the disk, which legitimate the Hamiltonian division approach discussed in Sec. (2). In addition, the deformation potential profiles shows that the strain effects cause an extra contribution on the energy splitting between $|s\rangle$ state and $|z\rangle$ state, which preforms on the splitting between conduction band and crystal-splitting band. Figure (6) shows the potential energy in xy -plane (left-hand side) and the decomposition of the overall potential energy into a piezoelectric and a pyroelectric components (right-hand side), which indicates that the built-in electric potential is mainly contributed by piezoelectric effects. In this case, the piezoelectric potential is about nine times larger than the pyroelectric potential. The modifications to the confinement potential by piezoelectric and pyroelectric effects are of the same order of magnitude as the material band offsets.

Figure (7) shows the subband structures of a 6.24 nm width $\text{In}_{0.91}\text{Ga}_{0.09}\text{N}$ disk in the lateral direction. Notice that, the top four valence bands are double degenerate at the zone center which corresponds to the heavy-hole and light-hole bands, while the single-fold states corresponds to the crystal-splitting band. The crystal-splitting bands are pushed down on energy due to the deformation potential contributed from strain effect. Figure (8) shows the band profile in growth direction as well as the calculated electronic states in a $\text{In}_{0.91}\text{Ga}_{0.09}\text{N}$ QW structure.

Determination of Dominant Photon Absorption Process

In this section, we perform the TMM simulation, which is described in Sec. (3), to calculate the leaking rate spectra considering the full InN/InGaN disk-in-wire photodiode, and aim to

determine the dominant photon absorption process to the photocurrent. Given the indium mole fraction at the disk region, strain-induced deformation potential, and the polarization field obtained from single disk-in-wire calculation, one can easily build up the full-device structure by repeating the potential profile of single disk-in-wire structure (four times corresponds to four disks in one nanowire structure), and sandwiched by graded-index p- and n-doped layers according to the epitaxial structure in Ref. 11. To incorporate the field which is contributed from both the external bias and the built-in potential of the p-i-n structure, we use the self-consistent transport model based on NEGF to estimate the band-bending effect induced from both carrier injection and doping concentration. Figure (9) shows both flat-band diagram and the band diagram under non-equilibrium condition. Notice that, due to the unintentionally n-doped concentration from nitrogen atom, the central intrinsic region is assumed to have $7.5 \times 10^{-16} \text{ cm}^{-3}$ n-doped concentration. This unintentionally n-doped concentration is of important since it influences not only the band diagram in the active region, but also the relative band bending between the active region and contact, and further effects the tunnelling behaviour of carriers.

Given the self-consistent potential under non-equilibrium condition considering spatial dependent doping profile, one can calculate the leaking rate spectra by using EBOM-based TMM described in Sec. (3). Figure (10a) shows the reflection spectra or the leaking rate spectra of the $\text{In}_{0.91}\text{Ga}_{0.08}\text{N}/\text{In}_{0.4}\text{Ga}_{0.6}\text{N}$ disk-in-wire guided-wave photodiode at zone center ($k_x = k_y = 0$). Figure (10b) and (10c) show the first three quasi-bound states corresponding to the first three deeps in the leaking rate spectra (10a), the top hole bound states, as well as the electronic bound states at each QW region. By examining the energy separations between bound states and quasi-bound states, one can determine the possible photon absorption process in such structure.

There are typically three major mechanisms which contributes photocurrent, and one can roughly distinguish them by examining the energy separation and photocurrent peak positions. The first one is phonon-assisted tunnelling, namely, carriers in the confinement

region jump into quasi-bound state and further escape from the active region by absorbing phonons. In this case, the energy separation between the bound and quasi-bound state should match the energy of optical phonon in the material, and the photocurrent peak positions are determined by the single-photon absorption (SPA) process involving with bound states. The second mechanism is simply the single-photon absorption process, which the electron transits into quasi-bound state in conduction band and contribute to photocurrent by considering certain tunnelling rate through the barrier. In this case, the photocurrent peak positions are determined by the SPA spectra multiplied by tunnelling rate of each quasi-bound state. The third mechanism is two-photon absorption (TPA) process. The electron initially in the valence band or conduction band, and jump into quasi-bound states by absorbing two photons. In our case, only the TPA process with identical photon energy are considered due to the experimental setup. In this case, the photocurrent peak positions are determined by single photon energy.

From the left-hand side of Fig. (10), one can see that the energy separation between top electron state and the bottom quasi-bound state (i.e. the quasi-bound state with the lowest energy) is 0.1478 eV, which is much larger than the optical-phonon energies in bulk InN (73 meV) and GaN (91 meV). This indicates that the phonon-assisted tunnelling is forbidden in the system. We hence look into SPA. The minimum possible SPA energy is the transition involving the first quasi-bound state and top hole state. Again, from Fig (10), the separation between these two state is $2.1152 - 0.4312 = 1.6840$ eV, which is much larger than the first measured photocurrent peak, which is around 1 eV. As a result, the dominant absorption process which contributes to the photocurrent is determined as the TPA. Notice that, the above analysis is focused on the photocurrent in low energy region (~ 1 eV), the SPA may still contribute to photocurrent in the higher energy region. As a result, both the SPA and TPA are considered in this work for calculating the photocurrent spectra generated by $\text{In}_{0.91}\text{Ga}_{0.09}\text{N}$ disk-in-wire photodiode.

Linear and Two-Photon Absorption

The optical properties of interest in TPA includes the inter-band transition and intra-band transition (between quantum disk states derived from the conduction band or valence band). Here we present a simple derivation for deducing the momentum dependent optical matrix elements from EBOM Hamiltonian. The detailed derivation for the case of ZB material is reported in Ref. 15. We summarize the key steps and extend into the version for WZ material by replacing the Hamiltonian.

The optical matrix elements between EBOM basis ($|s\rangle, |x\rangle, |y\rangle$, and $|z\rangle$) is given by

$$\frac{\hbar}{m_0} \langle \alpha', \mathbf{k} | \hat{\beta} \cdot \mathbf{p} | \alpha, \mathbf{k} \rangle = i \langle \alpha', \mathbf{k} | \hat{\beta} \cdot [H, \vec{\rho}] | \alpha, \mathbf{k} \rangle = i \langle \alpha', \mathbf{k} | \hat{\beta} \cdot [H_{ebom}^{8 \times 8}, \vec{\rho}] | \alpha, \mathbf{k} \rangle. \quad (15)$$

where the unit vector $\hat{\beta}$ represents the polarization of the incident light. In the reciprocal space, we can write the position vector $\vec{\rho}$ as an operator $i\nabla_{\mathbf{k}}$, and hence we have

$$[H_{ebom}^{8 \times 8}, \vec{\rho}] = -i \nabla_{\mathbf{k}} H_{ebom}^{8 \times 8}(\mathbf{k}), \quad (16)$$

which leads to an simple analytic expression suitable for \mathbf{k} in full BZ,

$$P_{\beta}^{\alpha, \alpha'}(\mathbf{k}) = \hat{\beta} \cdot \nabla_{\mathbf{k}} H_{ebom}^{8 \times 8}(\mathbf{k}). \quad (17)$$

Notice that Eq. (17) can be used for the calculation of both inter-band transition and intra-band transition.

Given the optical matrix elements, we can investigate the optical properties of $\text{In}_x\text{Ga}_{1-x}\text{N}$ QW by the dielectric function $\epsilon \equiv \epsilon_1 + i\epsilon_2$. The imaginary part ϵ_2 for the polarization is

given by²⁸

$$\begin{aligned}\epsilon_2(\omega) &= \frac{2\pi e^2}{V\omega^2} \sum_{\mathbf{k}_{||}; i, j} |\langle \mathbf{k}_{||}, i | P_\beta | \mathbf{k}_{||}, j \rangle|^2 \delta(E_j(\mathbf{k}_{||}) - E_i(\mathbf{k}_{||}) - \hbar\omega) \\ &= \frac{e^2}{2\pi d\omega^2} \sum_{i, j} \int d^2 k_{||} |\langle \mathbf{k}_{||}, i | P_\beta | \mathbf{k}_{||}, j \rangle|^2 \delta(E_j(\mathbf{k}_{||}) - E_i(\mathbf{k}_{||}) - \hbar\omega)\end{aligned}, \quad (18)$$

where $|\mathbf{k}_{||}, i\rangle$ denotes the i th electronic state of the quantum well associated with wave vector $\mathbf{k}_{||}$, $\hbar\omega$ denotes the photon energy, and V denotes the volume of the slab, which can be written as the cross-sectional area multiplied by the slab thickness. Due to the translational invariance in the lateral direction (x, y), the summation over $\mathbf{k}_{||}$ is replaced by integral $A/4\pi^2 \int d^2 k_{||}$. The real part of the dielectric function (ϵ_1) can be obtained from the imaginary part (ϵ_2) by utilizing Kramers-Kronig relation. The absorption coefficient is related to $\epsilon_2(\hbar\omega)$ by

$$\alpha(\hbar\omega) = \frac{\omega}{cn_r} \epsilon_2(\hbar\omega), \quad (19)$$

where c is the speed of light, n_r is the refractive index of the active material.

The TPA coefficient (β_2) for the QW is given by²⁹

$$\beta_2 = \frac{8\pi\omega}{c^2\epsilon_1(\omega)V} \sum_{\mathbf{k}_{||}, mn} |M_{mn}(\mathbf{k}_{||})|^2 \times \delta[2\hbar\omega - E_n(\mathbf{k}_{||}) + E_m(\mathbf{k}_{||})], \quad (20)$$

where

$$M_{mn}(\mathbf{k}_{||}) = 2\left(\frac{e}{m_e\omega}\right)^2 \sum_s \frac{\langle n\mathbf{k}_{||} | \hat{\epsilon} \cdot \mathbf{p} | s\mathbf{k}_{||} \rangle \langle s\mathbf{k}_{||} | \hat{\epsilon} \cdot \mathbf{p} | m\mathbf{k}_{||} \rangle}{\hbar\omega - [E_s(\mathbf{k}_{||}) - E_m(\mathbf{k}_{||})] + i\Gamma}. \quad (21)$$

$E_m(\mathbf{k}_{||})$, $E_s(\mathbf{k}_{||})$, and $E_n(\mathbf{k}_{||})$ denote the energies of initial, intermediate, and final state, respectively. The intermediate states, $|s\mathbf{k}_{||}\rangle$, can be either conduction or valence subband states. For simplicity, we have not included the effect of thermal excitation, although it is not negligible at finite temperature. Such an effect will be considered in a forthcoming paper. To avoid singularity comes from the denominator of the second-order perturbation theory, an imaginary number, ($i\Gamma$), is introduced in Eq. (21). The linewidth parameter Γ is

related to the finite lifetime of the QW states. All the optical constants for III-N materials used in this work are adopted from Ref 30.

In order to capture all possible transitions in the device, all the states correspond to different $|\mathbf{k}_{\parallel}\rangle$ s are required in the calculation of absorption. Due to high isotropic feature of both band structure and optical matrix elements for ZB crystal, for the device which is composed of ZB semiconductor, one can apply the angular average by adopting the \mathbf{k}_{\parallel} at a special angle $\phi = 22.5^\circ$ in k space. This angle is obtained by selecting the wavevectors in the midway between the [100] and [110] directions. In the other hand, both the band structure and optical matrix elements present strong anisotropy for WZ crystal. As a result, the transverse k integration can not be avoided in this case. There are several different ways to conduct the \mathbf{k}_{\parallel} integration, including the method of selecting special k point with different weighting base on the symmetry of crystal,³¹ or simple doing zone average in the desired portion of 1st BZ. In this work, we apply zone average method with area-dependent weighting to capture the full transition characteristics in the 1st BZ. Due to the C_3 symmetry of WZ crystal, we only sample the \mathbf{k}_{\parallel} in the triangle surrounded by Γ , K , and M points as shown in Fig (11).

The other effect which is introduced by the lateral confinement is the energy squeezing in the transverse k direction. In the disk-in-wire system, both the interface defined by the high-indium QD and the nanowire structure have confinement effect. For the InGa_N QD interface, the energy confinement accounts for the deformation potential induced by strain effect, piezoelectric field, and the material band offset. As for the interface at nanowire structure, only the material band offset contribute to the confinement effect. Note that the wire structure in our system is fairly large (radius = 26nm), the confinement effect is expected to be small, and the distribution of available \mathbf{k}_{\parallel} states in wavevector space is expected to be approximately continuum. However, in the low energy region, where the spacing between available \mathbf{k}_{\parallel} state are relatively large, it introduce forbidden band areas and makes noticeable modification to the absorption spectra. On the left-hand side of Fig.

(12), we show the distribution of available \mathbf{k}_{\parallel} for a nanowire structure with radius equals to 26.053 nm, which are generated by Bessel functions with vanishing boundary condition:

$$J_n(k_{\rho, nm}), \quad (22)$$

where

$$k_{\rho, nm} = \frac{x_{nm}}{r_b}. \quad (23)$$

The way we incorporate the energy squeezing effect is based on the crystal truncation method,³² namely, by selecting out available \mathbf{k}_{\parallel} , which satisfy the lateral confinement structure, to form the subband structure in the transverse k direction. In this work, we first generate a curve along radial direction as the right-hand side in Fig. (12), which corresponds to the lateral density of state. We then conduct interpolation to obtain the the weighting factor which accounts to the lateral density of state at each sampling mesh points of \mathbf{k}_{\parallel} . One can see from the right-hand side of Fig. (12), due to large state spacing at low energy region, the weighting factor that introduces the correction of lateral confinement is relatively large near the zone center. Up to now, we have introduced two weighting factors: one accounts to the zone integral effects while another one accounts to the energy squeezing effect induced from lateral confinement.

Photon Density of State in Graded-Index Waveguide

The graded-index layers of epitaxial design in the considered InN/InGaN disk-in-wire photodiode allows photon with only certain energies to propagate in the layer of nanowire arrays. The peaks of the photocurrent spectra happen when the photon DOS is at resonance with the absorption spectra, which indicates good electron-photon couplings in the active region. As a result, the DOS of optical waves propagating in the photodiode can also influence the peaks positions in the photocurrent spectra.

We calculate the complex-band structure of optical mode in the $\text{In}_{0.91}\text{Ga}_{0.09}\text{N}/\text{In}_{0.4}\text{Ga}_{0.6}\text{N}$ dsik-in-wire photodiode base on RCWA, which are shown in Fig (13) for both TE (y -polarization) and TM (z -polarization). Each point in Fig. (13) corresponds to a propagation mode in the $\text{In}_{0.91}\text{Ga}_{0.09}\text{N}/\text{In}_{0.4}\text{Ga}_{0.6}\text{N}$ dsik-in-wire waveguide with certain propagation constants. The gray shadow in the background corresponds to the intrinsic bulk material modes which propagates in silicon substrate and air. The dark curves correspond to the dispersion of guided-wave considering the graded-index structure. The dispersion curves in the region with sharp edges represent the well-guided mode in the device, while in the regions where the dispersion curves are divergent, the photon are more absorbing which are identified as resonance modes. Notice that, the photons that are involving in the optical transition process are not the well-guided ones. The well-guided optical mode only propagate in the device but never being absorbed and contribute to the photocurrent. The one which contribute to the optical transition is the photon corresponding to resonance mode. These photons propagate in the active layers with relatively small group velocity, and hence higher possibility of being absorbed. Besides that, the photon with small propagation constant (below air light-line) tend to have relatively large DOS due to the slope of the dispersion curve near zone-center, especially for TM mode.³³ As a result, we quantitatively characterize the photon DOS by the segment of dispersion curve below the air light-line. We use Lorentzian functions to fit the photon DOS for each resonance mode, which the peak of the Lorentzian function corresponds to the cut-off energy and the broadening are determined by the width of the divergence for the dispersion curve near the zone center. Figure (14) select out the modes which the wavefunction overlapping with nanowire layer higher than 3.8% for TE mode, and 4.3% for TM mode, which sketch out the dispersion curve of optical mode propagating in nanowire layer. From Fig. (14), we determine the cut-off energies of the modes that are interested as 0.95 eV, 1.38 eV, 1.62 eV, and 2.06 eV, while the corresponding broadening are 0.4 eV, 0.9 eV, 0.4 eV, and 1.7 eV, respectively. The fundamental mode and first excited modes for both TE and TM modes are not selected due to poor overlap with TPA absorp-

tion spectra. Notice that both in TE and TM cases, a resonance mode with 0.95 eV cut-off energy present in the complex-band structure of optical mode. As a result, the amplitude of the Lorentzian function which describes the DOS corresponding to this specific resonance mode are twice as the others in this work.

Result and Discussion

We first discretize the continuum states within the 30% of BZ into 55 sampling points. We then calculate the reflection spectra at each sampling \mathbf{k}_{\parallel} by using EBOM-based TMM described in Sec. (3). In Fig. (15), we show the reflection spectra with the energy imaginary part equals to 10 meV for certain sampling wavevectors. Each deep in the reflection spectra corresponds to strong absorption at that energy, and indicates the existence of quasi-bound or even bound state. We then collect the energies and wavefunctions corresponding to these deeps and construct a set of quasi-bound states, which serve as available tunnelling channels for carrier to reach contact. As for the calculation of absorption spectra, since the experiment was conducted with the light incident from the yz facet, we only considered the absorption corresponding to y -polarized and z -polarized photon. By multiplying the leaking rate of the tunnelling state which represents as a available channel in various optical transition process, the strength of the photocurrent spectra is obtained.

Figure (16) shows the photocurrent spectra via SPA of the $\text{In}_{0.91}\text{Ga}_{0.09}\text{N}$ disk-in-wire structure. The whole spectra is broaden with $\sigma = 0.1$ eV due to inhomogeneity of the structure. As we expected, the first absorption peak present in the energy region is higher than 1.5 eV, which indicates that the measured photocurrent peaks in low energy region are attributed to some mechanism other than SPA. The SPA absorption may contribute to the photocurrent around 2 eV, which the dominant SPA process is the one with y -polarized photon.

The TPA can categorized into two different types depending on the selection of inter-

mediate state: VB-CB-CB, which uses subband state in the conduction band as intermediate state, while VB-VB-CB uses subband state in the valence band as intermediate state. Figure (17) show the photocurrent spectra via VB-CB-CB absorption of the $\text{In}_{0.91}\text{Ga}_{0.09}\text{N}$ disk-in-wire structure. The three packets feature for cases with both y -polarized photon and z -polarized photon presents in the calculated spectra, while the case of z -polarization is about 10 times stronger than the case of y -polarization. Figure (18) shows the photocurrent spectra induced by VB-VB-CB type transition. As you can see the VB-VB-CB TPA is generally stronger than VB-CB-CB TPA in low energy region due to higher DOS of valence subband. The photocurrent strength for the case of y -polarization and z -polarization are comparable for VB-VB-CB type transition, with the y -polarization induced strength is around 2.5 times stronger. Notice that, the first and second packets in the case of VB-CB-CB transition, and the packet below 1 eV in the case of VB-VB-CB transition, do not really satisfy the double-resonance condition of TPA, but being enhanced significantly by the ω^{-3} factor in the TPA formulation. This implies that the photocurrent peaks in the low energy region are pinned and less sensitive to external bias. From fig (17) and (18), we expect that the photocurrent spectra in the region between 1.2 eV to 2.5 eV are mainly contributed by VB-CB-CB, while VB-VB-CB transition is dominant in the low energy region (< 1 eV).

Figure (19) shows the total photocurrent spectra with and without considering the photon DOS, as well as the comparison with the experimental data. Notice that, in order to compare the calculated photocurrent spectra with experimental data, an energy-depedent curve as shown on the right hand side in Fig (19), which characterize the intensity distribtuion of light source and the response grating efficiency are adopted from equipment specification and incorporated in the calculation. In the case without incorporating photon DOS, only certain peaks appear in the calculated spectra. The calculated phtocurrent spectra shows peaks at 0.806 eV, 1.287 eV, 1.914 eV, 2.009 eV, and 2.405 eV. The first peak corresponds to TPA with VB-VB-CB transition, which presents in the measured photocurrent spectra under -0.1 V and merged into the peak at ~ 1 eV under -1 V external bias. The second

and last peak corresponds to TPA with VB-VB-CB transition, while peaks around 2 eV are induced by SPA. After including the photon DOS correction, a large peak presents at 0.95 eV, which corresponds to TPA with VB-VB-CB transition coupling with both TE/TM photon DOS. The original peak at 1.287 eV in the case without photon DOS correction becomes a small shoulder as shown in the measured data, while another peak appears at 1.38 eV. Besides that, a peak appears at 1.62 eV after considering the photon DOS. However, due to small absorption strength around 1.5 eV to 1.8 eV, it merges into the second packet in the measured data. Notice that the deviation of the line-shape between the calculated spectra and the measured data between 1.2 eV and 1.9 eV attribute to the approximation of photon DOS using Lorentzian function. It may be improved by incorporating the actual photon DOS from the resonance mode dispersion curve. The second last peak at 2.039 eV corresponds to VB-CB-CB transition peak at 2.066 eV coupling with z-polarized photon. the very last peak at 2.375 eV corresponds to the non-coupling peak at 2.296 eV with TPA VB-CB-CB transition in the measured photocurrent spectra. A peak corresponds to SPA presents at 1.91 eV in the calculated spectra may attribute to the error that is introduced when incorporating photocurrent strength with SPA component and TPA component, which a more accurate estimation of light intensity contribute to the nanowire layer is required.

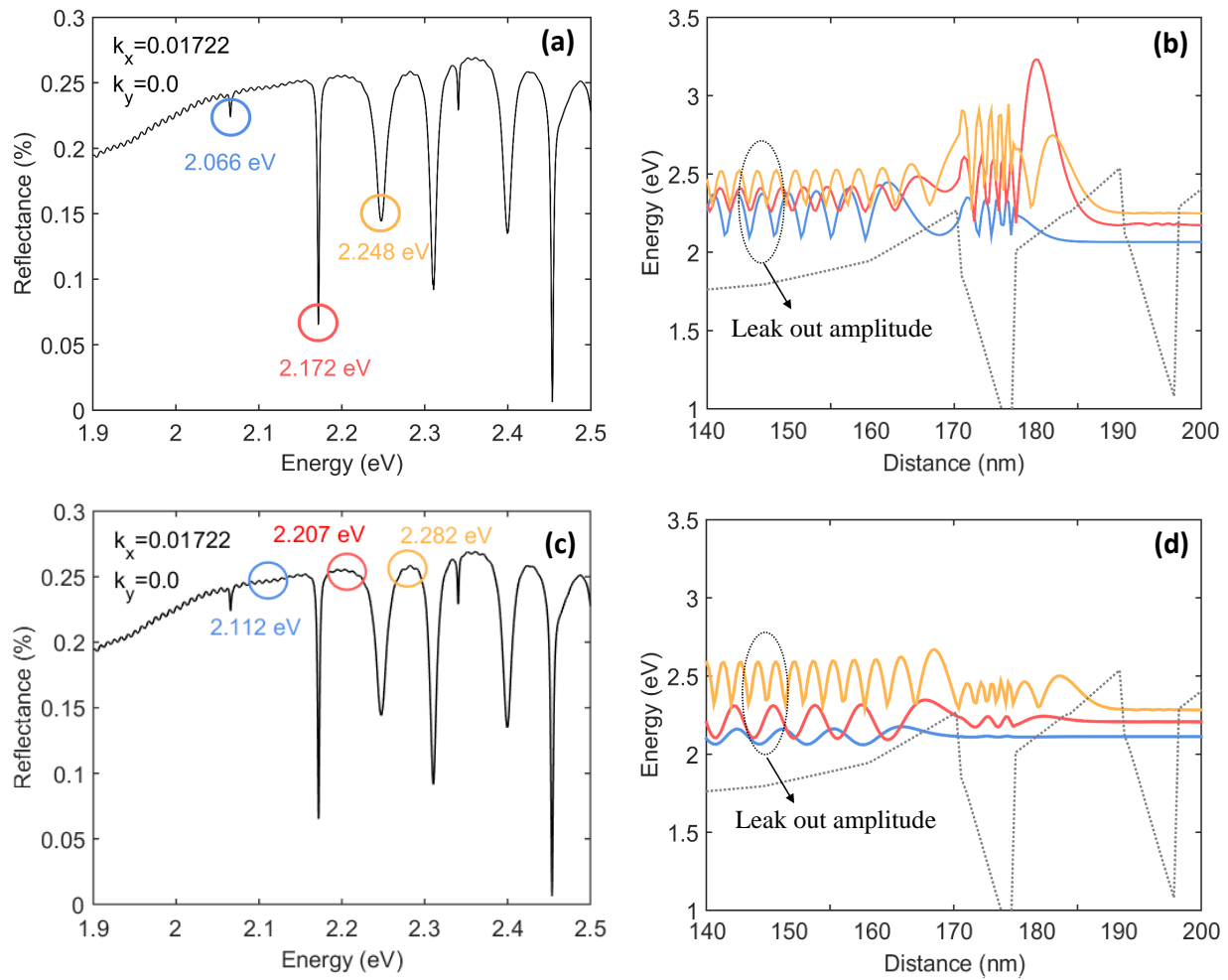


Figure 1: Demonstration of calculated leaking rate spectra and the corresponding wavefunctions of InN/InGaN multi-QW structure by EBOM-based TMM.

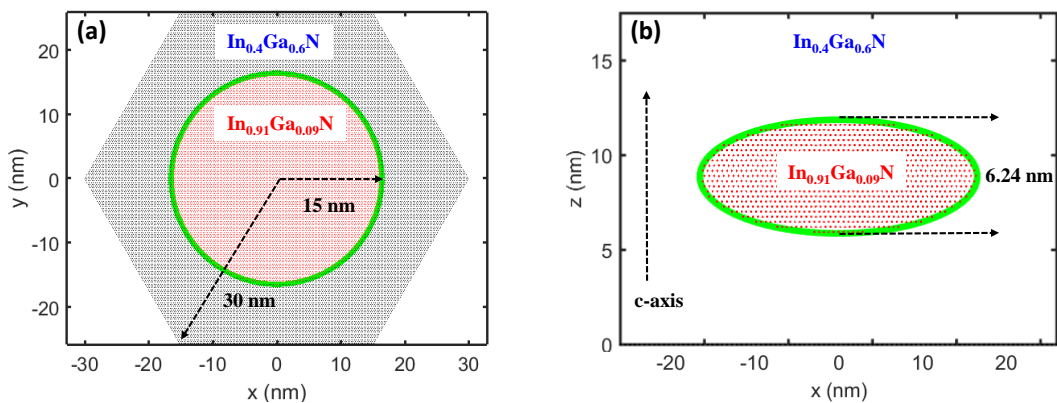


Figure 2: Input geometry of the $\text{In}_x\text{Ga}_{1-x}\text{N}$ disk buried in $\text{In}_{0.4}\text{Ga}_{0.6}\text{N}$ structure for the VFF model.

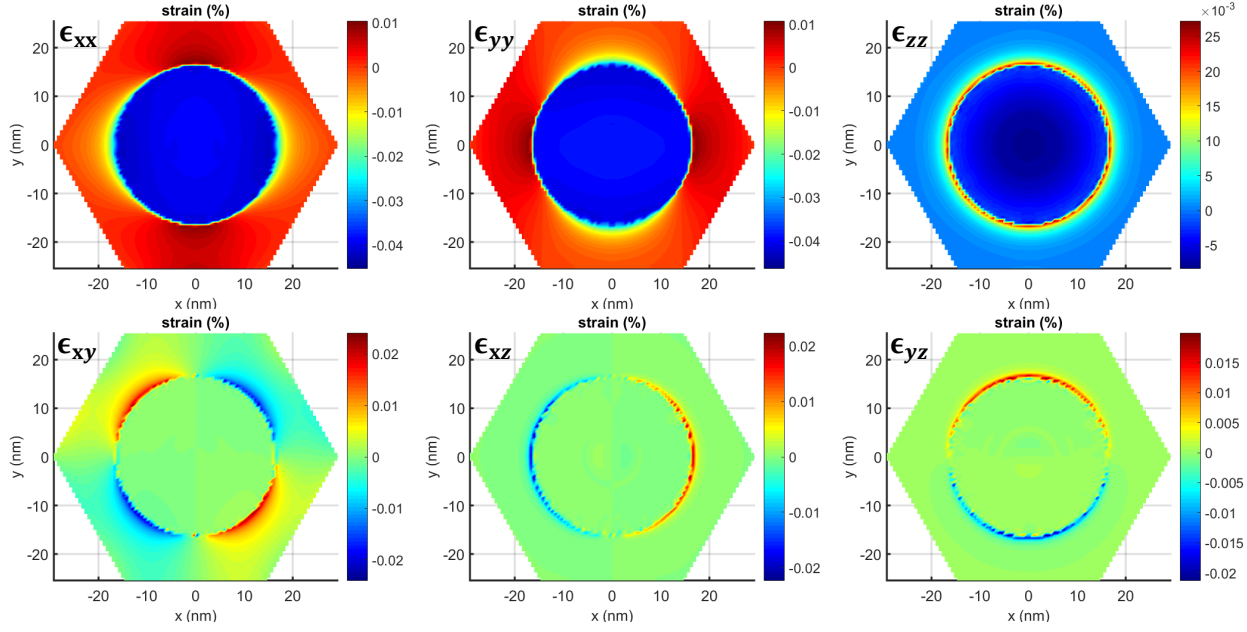


Figure 3: Calculated strain distribution in a $\text{In}_{0.91}\text{Ga}_{0.09}\text{N}$ disk with 6.24 nm height in the plane of 8.64 nm.

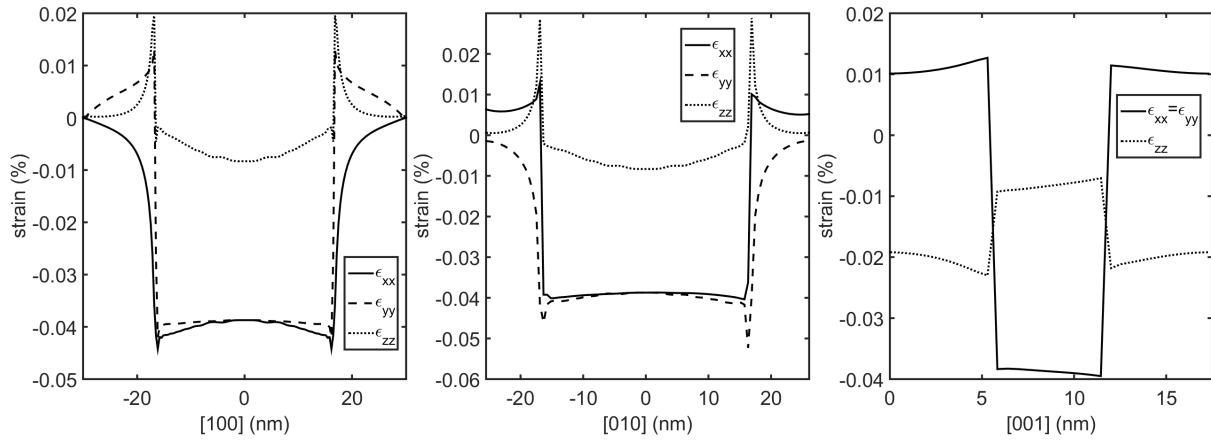


Figure 4: Calculated strain distribution in a $\text{In}_{0.91}\text{Ga}_{0.09}\text{N}$ dot with 6.24 nm height in the plane of 8.64 nm. The solid line is for ϵ_{xx} , dashed line for ϵ_{yy} , and dotted line for ϵ_{zz} .

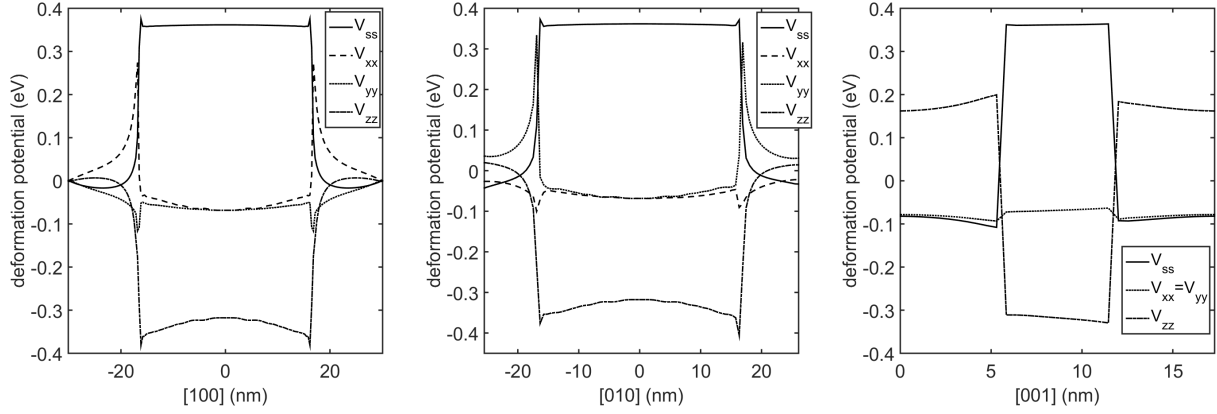


Figure 5: Diagonal elements of the deformation potential for $\text{In}_{0.91}\text{Ga}_{0.09}\text{N}$ disk with 6.24 nm height in the plane of 8.64 nm. The solid line is for V_{ss} , dashed line for V_{xx} , dotted line for V_{yy} , and dot-dashed line for V_{zz} .

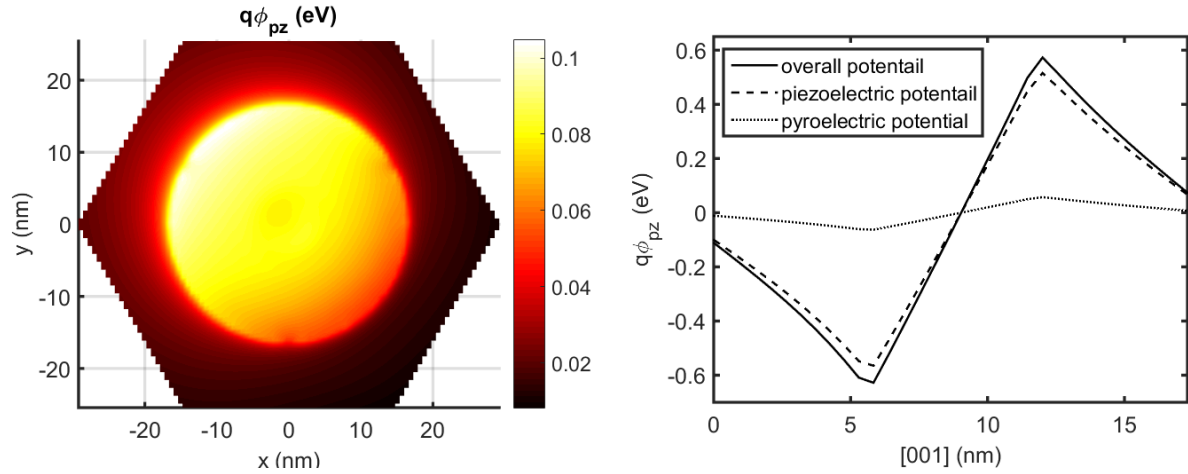


Figure 6: Calculated built-in electric potential in a $\text{In}_{0.91}\text{Ga}_{0.09}\text{N}$ disk with 6.24 nm height. The overall electric potential in the plane of 8.64 nm (left-hand side). The linescan of the built-in potential along the [0001] direction through the disks' center (right-hand side), where the solid line shows the overall potential, and the dashed line and the dotted line show the components induced by the piezoelectric polarization and the pyroelectric polarization.

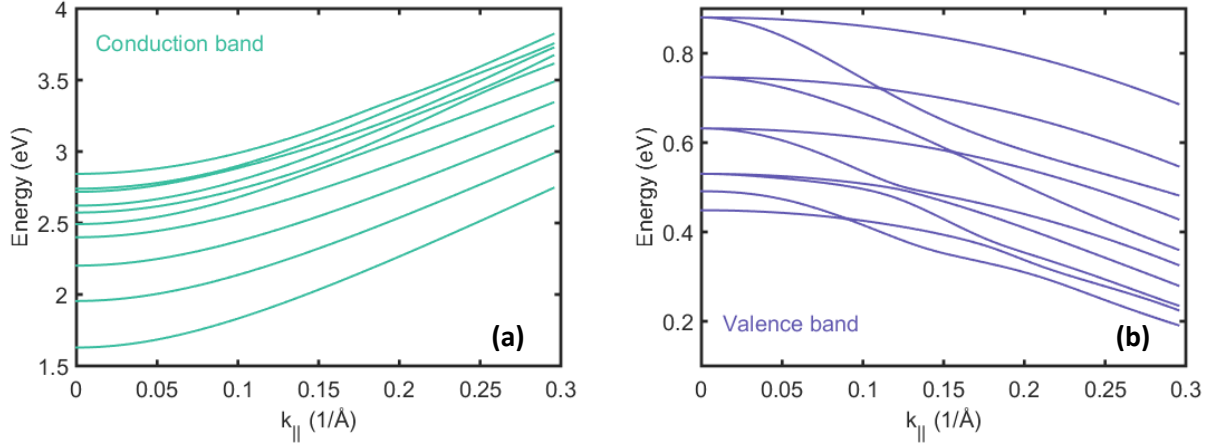


Figure 7: Conduction (left-hand side) and valence (right-hand side) band structures of a 6.24 nm width $\text{In}_{0.91}\text{Ga}_{0.09}\text{N}$ QW.

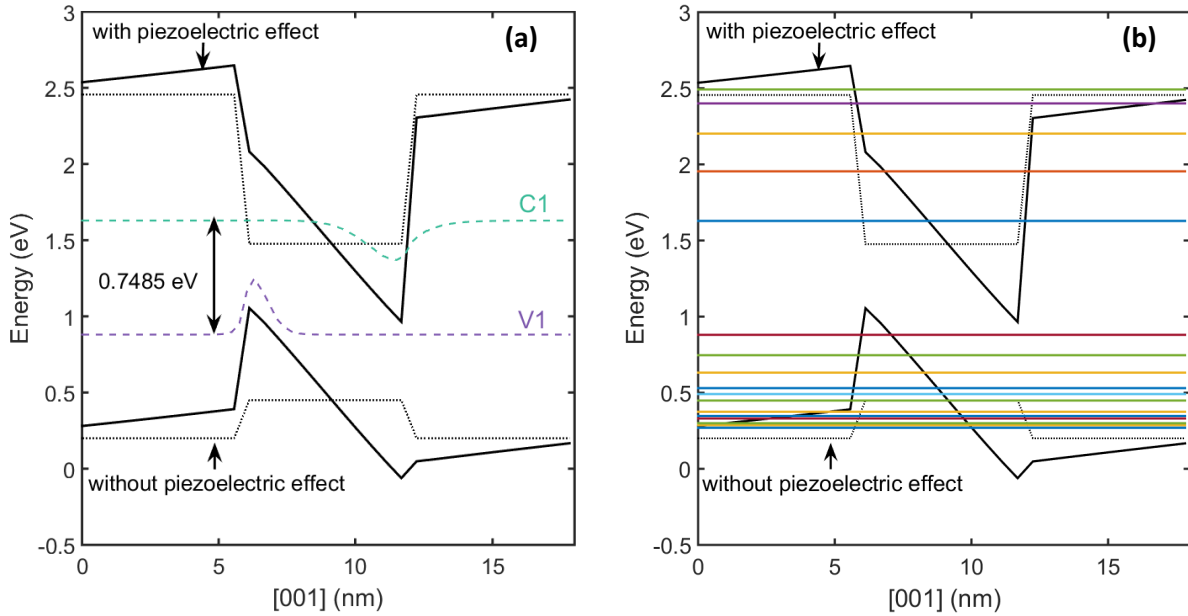


Figure 8: The lateral-average band profile w/o piezoelectric effect for a $\text{In}_{0.91}\text{Ga}_{0.09}\text{N}$ quantum well structure with 6.24 nm width. The corresponding ground state energies for conduction and valence band (left-hand side). The bottom 5 states in the conduction band and top 20 states in the valence band (right-hand side).

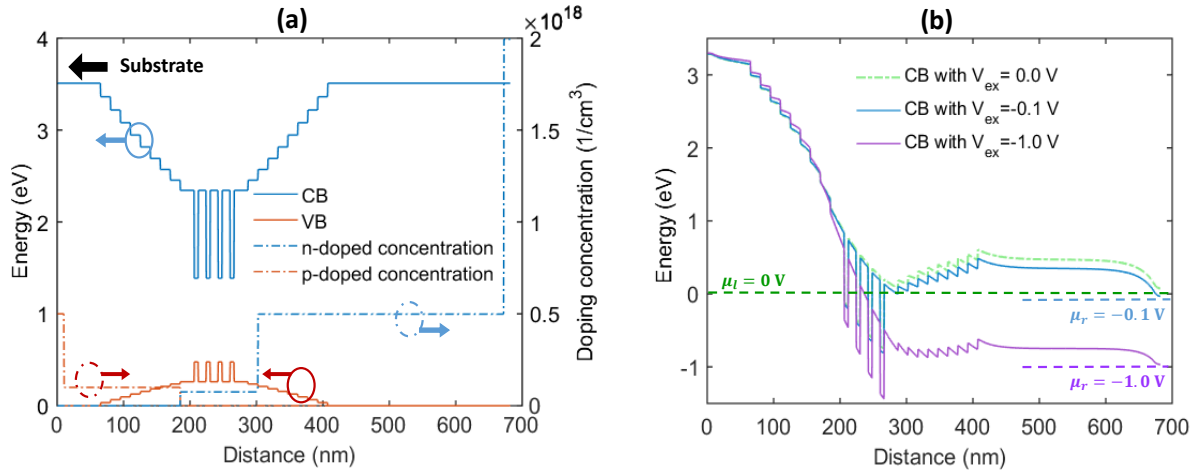


Figure 9: Flat band diagram for InGaN photodiode (left) and self-consistent band diagram under various external bias (right) calculated by NEGF.

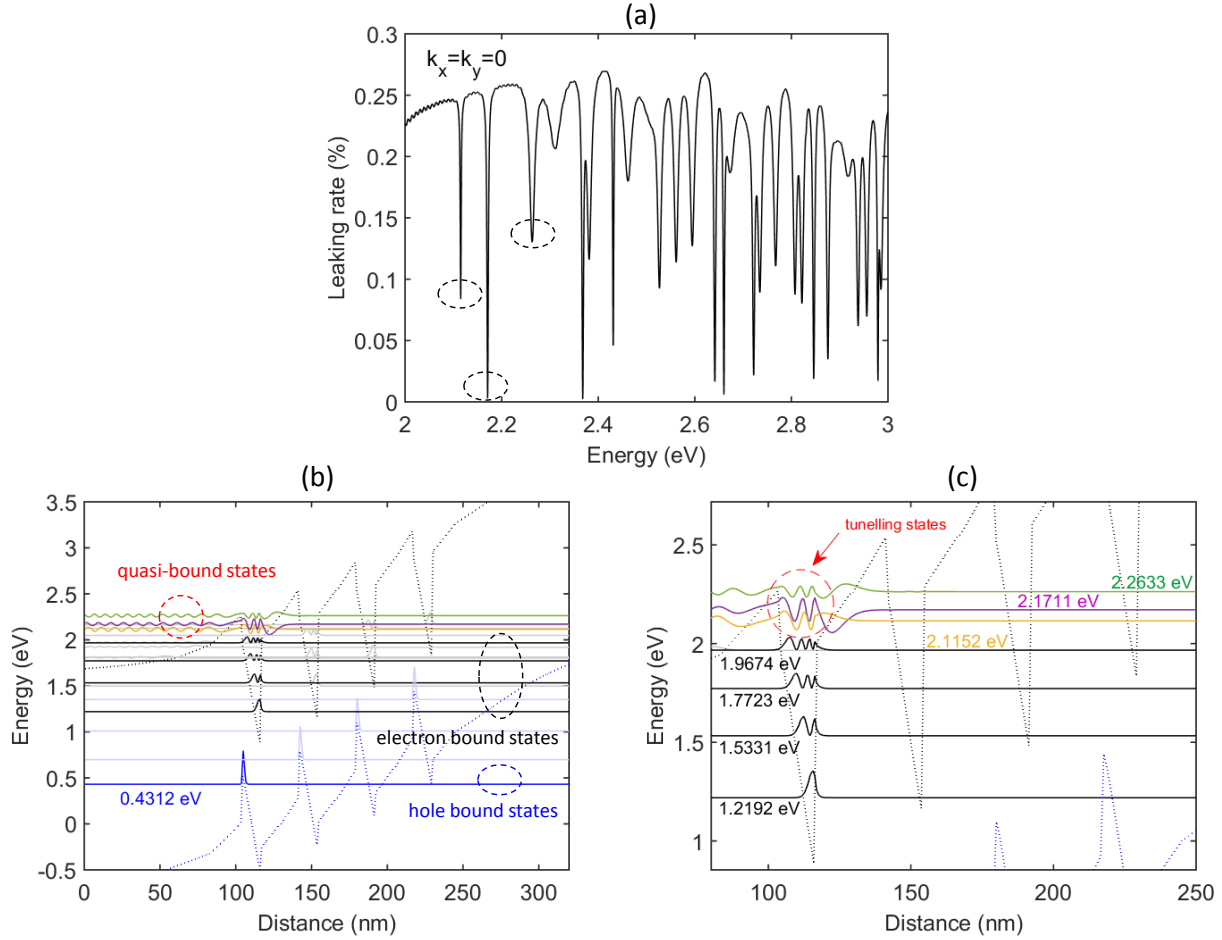


Figure 10: Leaking rate spectra and bound states in the $\text{In}_{0.91}\text{Ga}_{0.08}\text{N}/\text{In}_{0.4}\text{Ga}_{0.6}\text{N}$ multi-QW structure at zone center. (a) The leaking spectra calculated by TMM. (b) First three quasi-bound states and bound states in multi-QW region. (c) Zoomed-in figure for the quasi-bound states and bound states in multi-QW region.

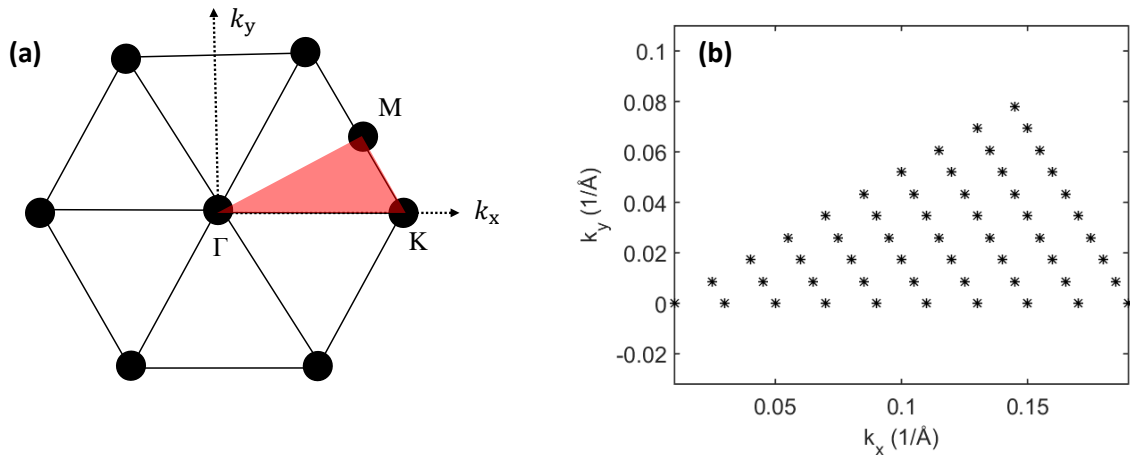


Figure 11: Sampling area (left) and sampling \mathbf{k}_{\parallel} points in 1st BZ (right).

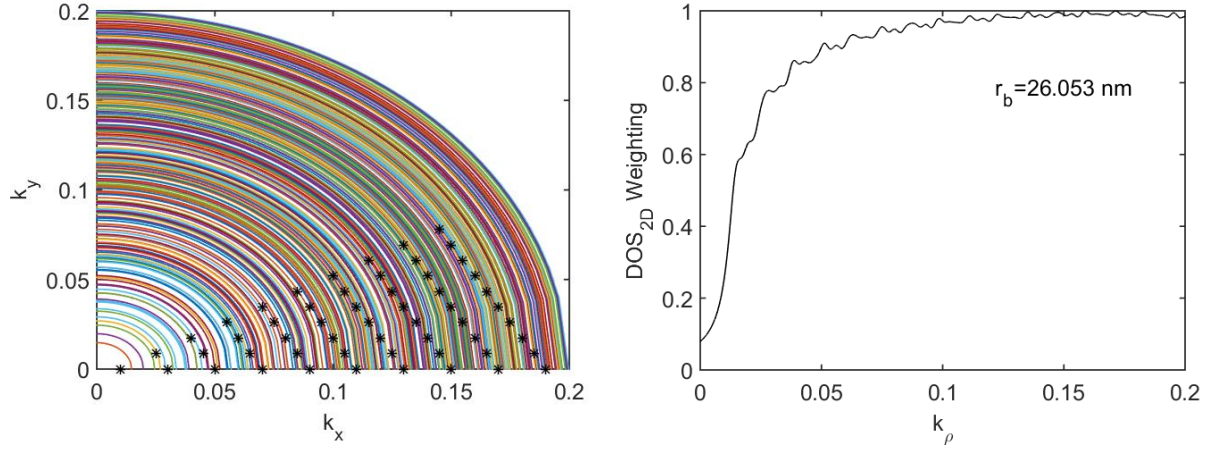


Figure 12: Discretized states introduced by lateral confinement (left), and weighting factor curve corresponds to density of state in lateral direction for $r_b = 26.053$ nm.

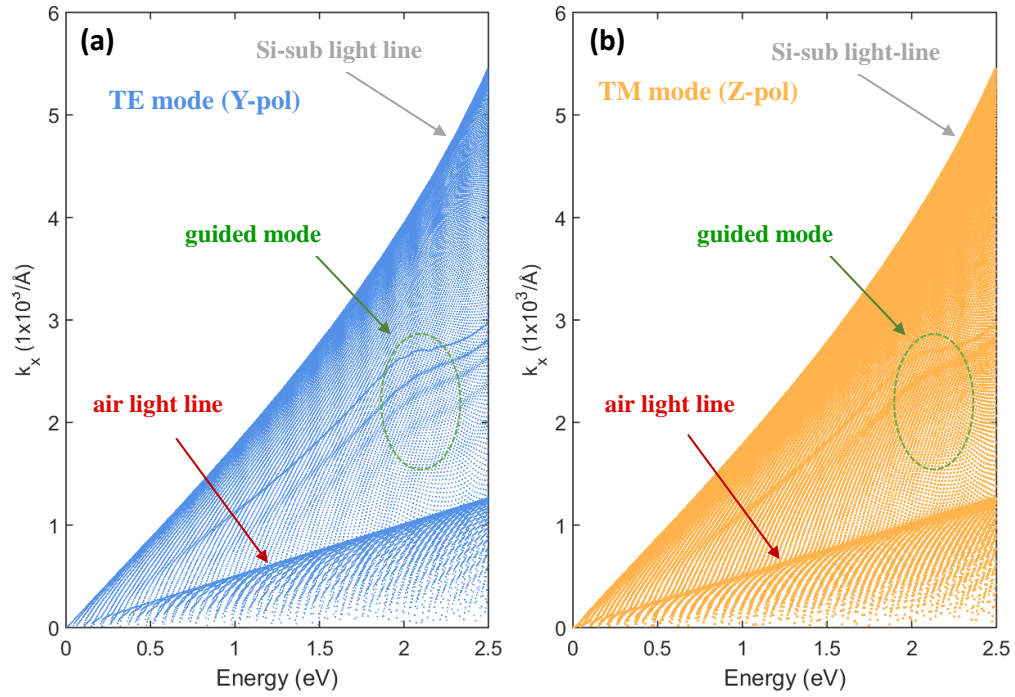


Figure 13: TE and TM mode components of complex-band structure for optical modes in the $\text{In}_{0.91}\text{Ga}_{0.09}\text{N}/\text{In}_{0.4}\text{Ga}_{0.6}\text{N}$ graded-index waveguide structure.

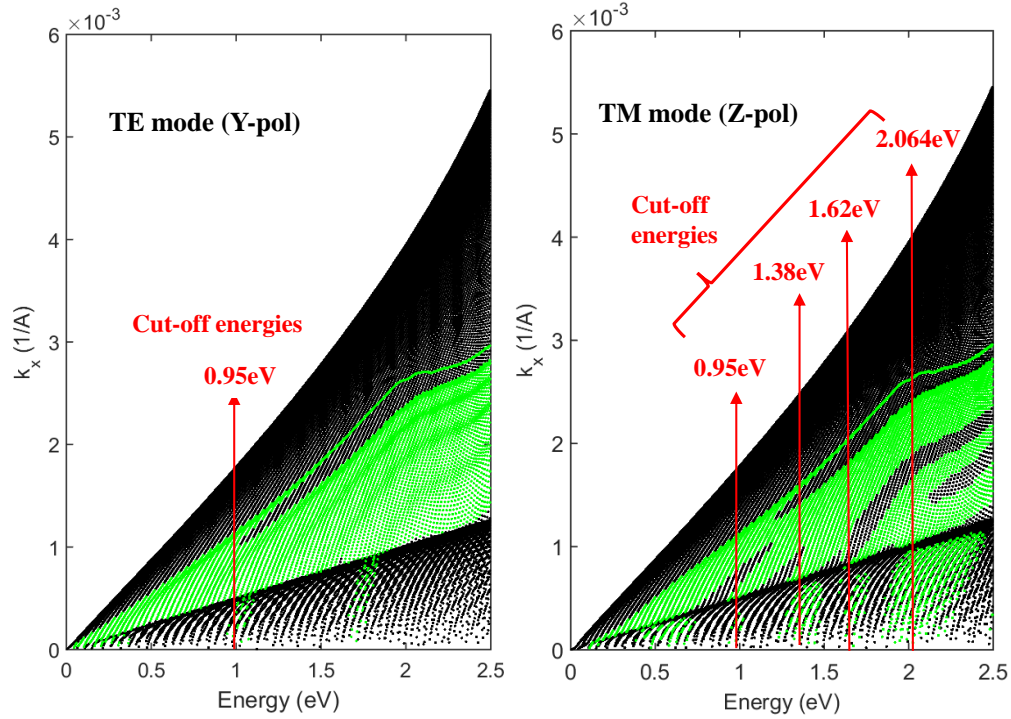


Figure 14: TE and TM mode components of complex-band structure for optical modes in the $\text{In}_{0.91}\text{Ga}_{0.09}\text{N}/\text{In}_{0.4}\text{Ga}_{0.6}\text{N}$ graded-index waveguide structure with the mode propagating in nanowire layer are selected out in green.

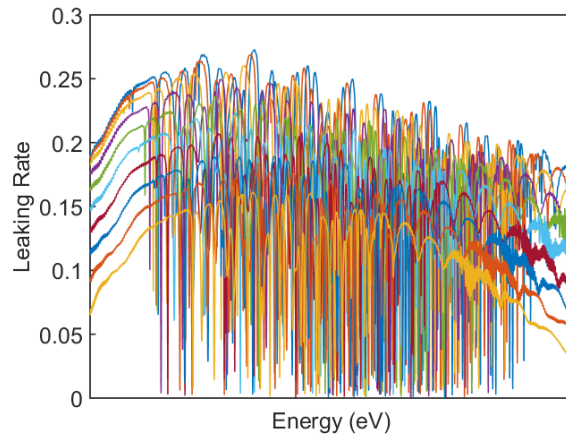


Figure 15: Reflection coefficients or leaking rate spectra with various k_{\parallel} calculated by TMM with EBOM.

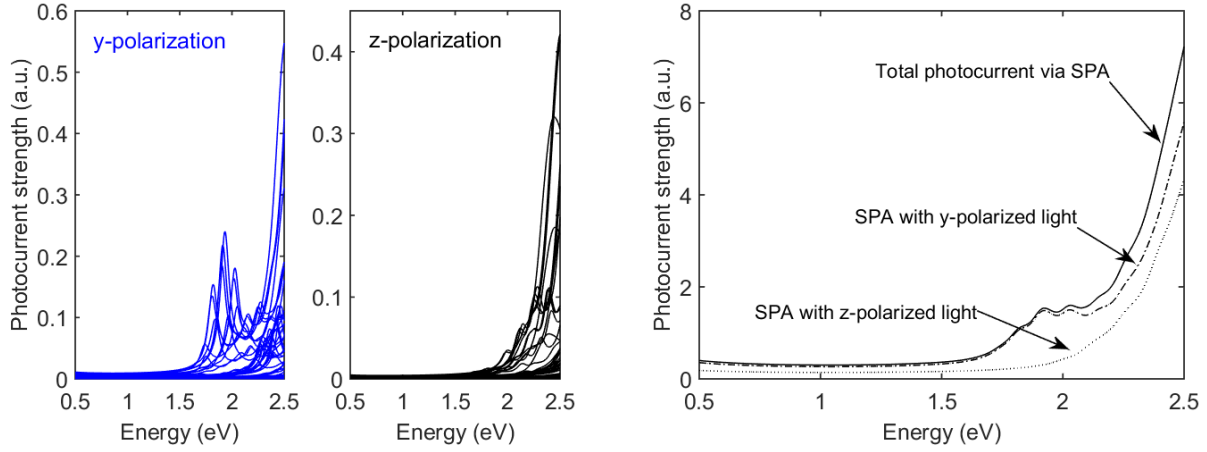


Figure 16: Photocurrent spectra via SPA process with both y-polarization and z-polarization light for each sampling $k_{||}$ (left), and total photocurrent spectra via SPA (right).

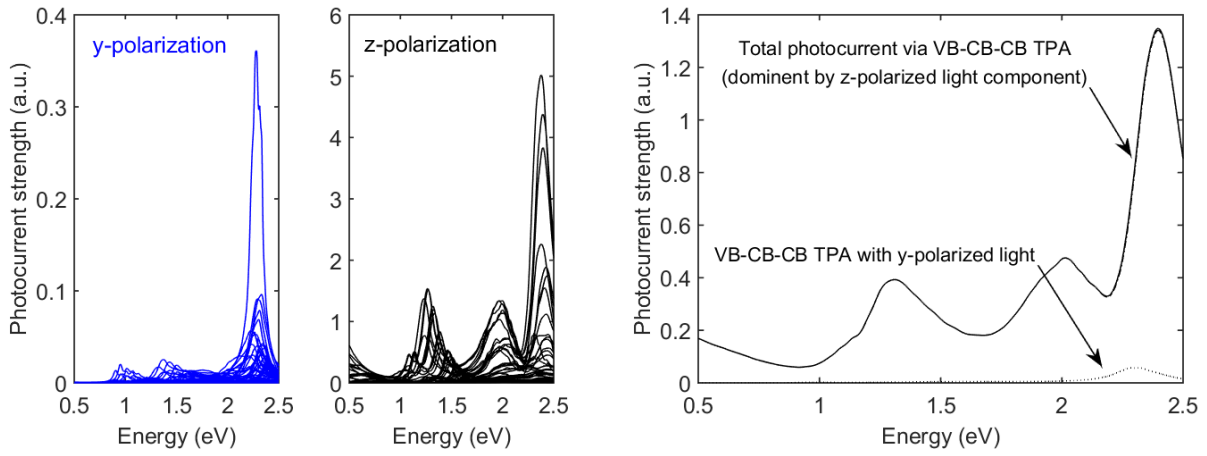


Figure 17: Photocurrent spectra via VB-CB-CB TPA process with both y-polarization and z-polarization light for each sampling $k_{||}$ (left), and total photocurrent spectra via VB-CB-CB TPA (right).

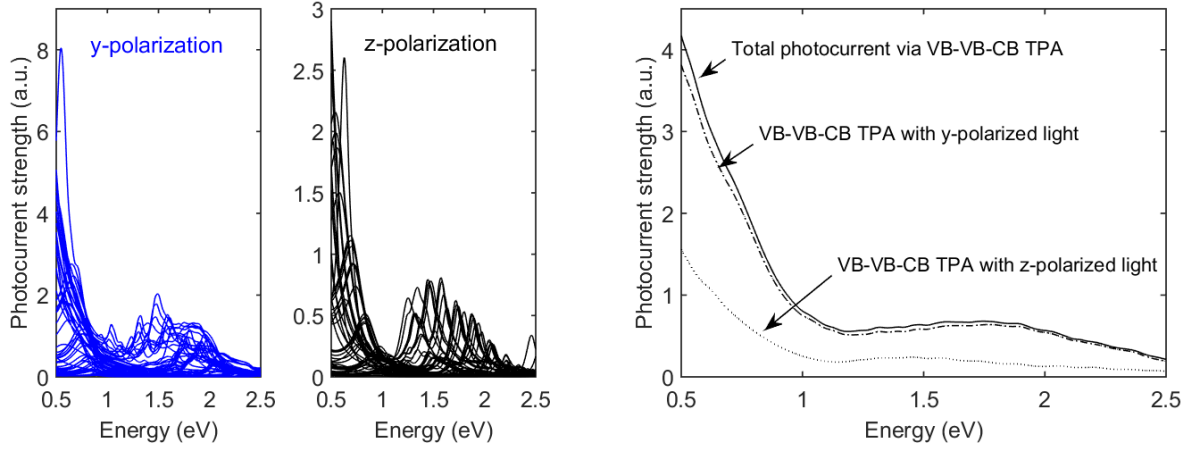


Figure 18: Photocurrent spectra via VB-VB-CB TPA process with both y-polarization and z-polarization light for each sampling \mathbf{k}_{\parallel} (left), and total photocurrent spectra via VB-VB-CB TPA (right).

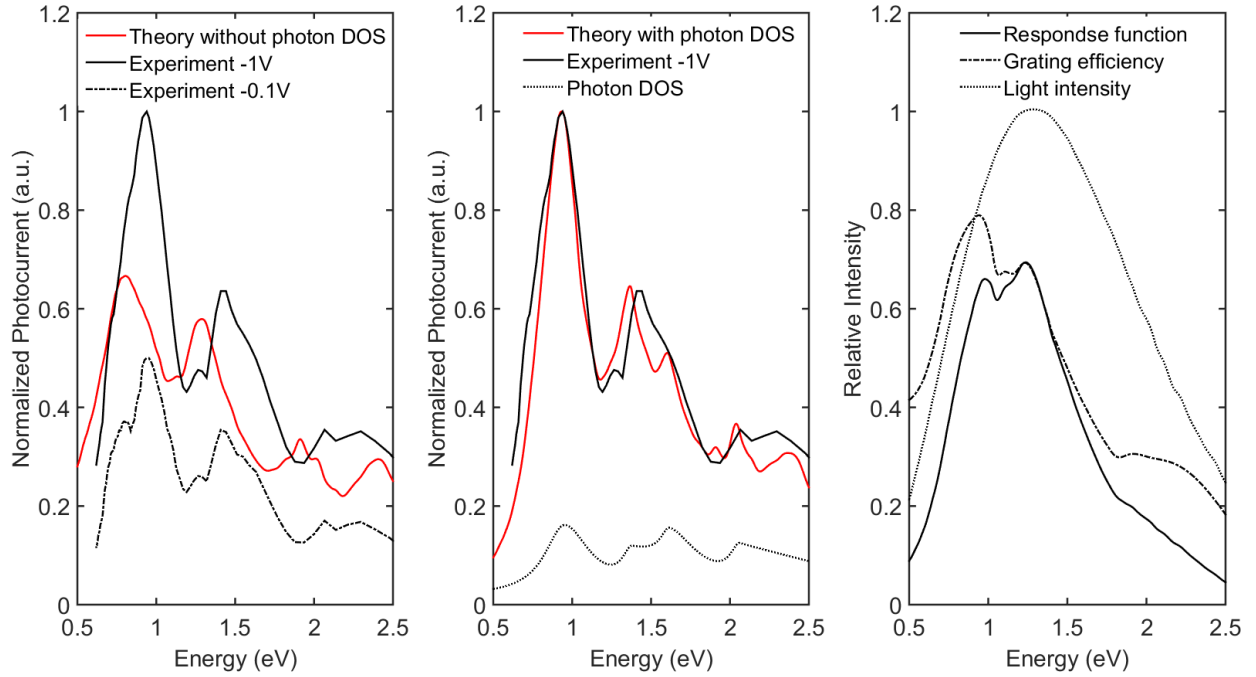


Figure 19: Calculated photocurrent spectra and the comparison with experimental data (left and middle). The equipment response function used in this work (right).

Acknowledgement

References

- (1) A. W. Fang, H. Park, O. Cohen, R. Jones, M. J. Paniccia, and J. E. Bowers, *Opt. Express* **14**, 9203–9210 (2006) .
- (2) D. Liang, and J. E. Bowers, *Nat. Photonics* **4**, 511–517 (2010) .
- (3) S. Tanaka, S.-H. Jeong, S. Sekiguchi, T. Kurahashi, Y. Tanaka, and K. E. Morito, *Opt. Express* **14**, 9203–9210 (2006) .
- (4) A. Y. Liu, C. Zhang, J. Norman, A. Snyder, D. Lubyshev, J. M. Fastenau, A. W. Liu, A. C. Gossard, and J. E. Bowers, *Appl. Phys. Lett.* **104**, 041104 (2014) .
- (5) Z. Mi, P. Bhattacharya, J. Yang, and K.P. Pipe, *Electron. Lett.* **41**, 742–744 (2005) .
- (6) H.Z. Chen, A. Ghaffari, H. Wang, H. Morkoc, and A. Yariv, *Appl. Phys. Lett.* **51**, 1320–1321 (1987) .
- (7) S. Jahangir, T. Schimpke, M. Strassburg, K. A. Grossklaus, J. M. Millunchick, and P. Bhattacharya, *IEEE J. Quantum Electron.* **50**, 530–537 (2014) .
- (8) S. Jahangir, M. Mandl, M. Strassburg, and P. Bhattacharya, *Appl. Phys. Lett.* **102**, 071101 (2013) .
- (9) H. P. Trung Nguyen, K. Cui, S. Zhang, S. Fatholouloumi, and Z. Mi, *Nanotechnology* **22**, 445202 (2011) .
- (10) W. Guo, M. Zhang, A. Banerjee, and P. Bhattacharya, *Nano Lett.* **10**, 3355–3359 (2010) .
- (11) A. Hazari, F.-C. Hsiao, L. Yan, J. Heo, J. M. Millunchick, J. M. Dallesasse, and P. Bhattacharya, *Nano Lett. IEEE J. Quantum Electron.* **53**, 1–9 (2017) .

- (12) S. R. White, and L. J. Sham, Phys. Rev. Lett. **47**, 879 (1981).
- (13) B. A. Foreman, Phys. Rev. B **56**, R12748 (1997).
- (14) Y.C. Chang, Phys. Rev. B **37**, 8215 (1988).
- (15) Y.C. Chang, and W. E. Mahmoud, Comput. Phys. Commun. **196**, 92 (2015).
- (16) F.-C. Hsiao, C.T. Liang, Y.C. Chang, and J. M. Dallesasse, Comput. Phys. Commun. **252**, 107139 (2020).
- (17) M.G. Moharam, E. B. Grann, D. A. Pommet, and T.K. Gaylord, J. Opt. Soc. Am. **12**, 1068–1076 (1995).
- (18) P.N. Keating, Phys. Rev. B **145**, 637 (1966).
- (19) R. Martin, Phys. Rev. B **1**, 4005 (1970).
- (20) H. Jiang, and J. Singh, Phys. Rev. B **56**, 4696 (1997).
- (21) D. Camacho, and Y.M. Niquet, Physica E **42**, 1361–1364 (2010).
- (22) M. Mitchell, *Symmetry and Strain Induced Effects in Semiconductors* (Wiley, Halsted, UK, 1974).
- (23) E. J. Austin, and M. Jaros, Phys. Rev. B **31**, 5569 (1985).
- (24) D. Ahn, and S. L. Chung, Phys. Rev. B **34**, 9034 (1986).
- (25) V. A. Mandelshtam, T. R. Ravuri, and H. S. Taylor, Phys. Rev. Lett. **70**, 1932 (1993).
- (26) D. M. T. Kuo, and Y. C. Chang, Phys. Rev. B **61**, 11051 (2000).
- (27) DZ-Y. Ting, E. T. Yu, and T. C. McGill, Phys. Rev. B **45**, 3583 (1992).
- (28) F. Bassani, and G. P. Parravicini, *Electronic States and Optical Transitions in Solids* (Pergamon, New York, 1975).

- (29) Y. C. Chang, J. Cheung, A. Chiou, and M. Khoshnevisan, *J. Appl. Phys* **68**, 4233 (1990).
- (30) V. I. Gavrilenko, and R.Q. Wu, *Phys. Rev. B* **61**, 2632 (2000).
- (31) S. L. Cunningham *Phys. Rev. B* **10**, 4988 (1974).
- (32) D. J. Chadi, and Marvin L. Cohen, *Phys. Rev. B* **8**, 5747 (1973).
- (33) C. J. Chang-Hasnain, and W. Yang, *Adv. Opt. Photonics* **4**, 379–440 (2012).

Modeling Photocurrent Spectra of In_{0.91}Ga_{0.09}N/In_{0.4}Ga_{0.6}N Disk-in-Wire Photodiode on Silicon for 1.3 μm – 1.55 μm Operation

Fu-Chen Hsiao,^{*,†} Arnab Hazari,[‡] Pallab Bhattacharya,[‡] Yia-Chung Chang,[¶] and
John M. Dallesasse[†]

[†]*Department of Electrical and Computer Engineering, University of Illinois at
Urbana-Champaign, Urbana, Illinois 61801, United States*

[‡]*Department of Electrical Engineering and Computer Science, University of Michigan,
1301 Beal Avenue, Ann Arbor, Michigan 48109-2122, United States*

[¶]*Research Center for Applied Sciences, Academia Sinica, Taipei 11529, Taiwan*

E-mail: fhsiao3@illinois.edu

Abstract

This work reports comprehensive theoretical modeling of photocurrent spectra generated by an In_{0.91}Ga_{0.09}N/In_{0.4}Ga_{0.6}N disk-in-wire photodiode. The strain distribution is calculated by valence-force-field (VFF) model, while a realistic band structure of the InN/InGaN heterostructure is incorporated using an eight-band effective bond-orbital model (EBOM) with spin-orbit coupling neglected. The electrostatic potential is obtained from self-consistent calculation employing the non-equilibrium Green's function (NEGF) method. With the strain distribution and band profile determined, a multi-band transfer-matrix method (TMM) is used to calculate the tunneling coefficients of optically-pumped carriers in the absorbing region. The photocurrent spectra

contributed by both single-photon absorption (SPA) and two-photon absorption (TPA) are calculated. The absorption coefficient is weighted by the carrier tunneling rate and the photon density-of-state (DOS) in the optical cavity formed in the nanowire region to produce the photocurrent. The calculated photocurrent spectra is in good agreement with experimental data, while physical mechanisms for the observed prominent peaks are identified and investigated.

Introduction

Integration of III-V devices on silicon is a well-known technique for overcoming the low efficiency of photon-absorbing and emitting process in Si-based photonic devices.¹⁻³ The direct epitaxial growth of III-V materials and heterostructure on silicon appears to be the most straightforward method to achieve III-V on silicon integration.⁴⁻⁶ However, due to the high density of threading dislocations, mismatch of thermal expansion coefficients, and formation of antiphase domains, the direct epitaxial growth method encounters many problems that have not been properly resolved.

Instead of planar structures, growing nanowire structures consisting of III-nitride (III-N) semiconductors in WZ phases provides a very different means to deal with the problem of III-V/Si integration.⁷⁻⁹ Due to efficient lateral-strain relaxation at the nanowire-silicon interface, nanowire heterostructures show efficient reduction of polarization fields¹⁰ and achieve smaller radiative recombination time than a system with quantum well (QW) structures.⁷ From the simulation perspective, the modeling for high-indium-content III-N based device in the WZ phase presents multiple challenges. The ambiguity introduced by the ordering of the operators for kinetic energy may lead to spurious solutions in the $k \cdot p$ model,^{11,12} especially in the large wavevector region for high-indium-content devices due to the uncertainty of band parameters in InN. This indicates that a band structure model which is capable of producing accurate band structure in the full Brillouin Zone (BZ) is needed. Besides that, hexagonal structures present much lower symmetry (C_{3v}) than the cubic phase (T_d), which requires

extra fitting parameters for the band structure and effective-masses. As a result, a semi-empirical model which is capable of producing full-zone band structure and effective-masses close to experimental values near the zone center is needed. Furthermore, since the optical transition does not necessarily happen near the BZ center for high-indium-content devices, the optical matrix elements which includes wavevector dependence are required as well. Recently, a novel monolithic optical interconnect on (001)Si substrate using an InGaN disk-in-wire array, which consists of an edge emitting diode laser and guided wave photodiode, has been demonstrated experimentally.¹³ To the best of our knowledge, due to the complexity of the geometry, ultra-high indium content active region, and the requirement of a realistic band structure calculation within a large portion of first BZ, a systematic study of the photon absorption process as well as the carrier tunneling behaviors is not yet available.

In this work, we provide a comprehensive theoretical analysis for the photocurrent spectra of high-indium-content InN/InGaN disk-in-wire photodiodes with a guided wave structure base on the eight-band effective bond-orbital model (EBOM).¹⁴⁻¹⁶ The theoretical model takes into account the strain distribution, polarization field effect (piezoelectric and spontaneous), and realistic band structure of InN/InGaN with suitable boundary conditions for modeling quantum carrier transport. The photon density-of-states (DOS) which is sharply peaked at the resonance modes of the InN/InGaN waveguide structure is also incorporated in our model by using the rigorous couple-wave analysis (RCWA).¹⁷ These sharp peaks are fitted with Lorentzian functions centered at cut-off energies with resonance bandwidth. The simulation provides detailed descriptions on the corresponding optical transition process for each of the peaks on the photocurrent spectra. The calculated photocurrent spectra which includes both one-photon and two-photon absorption processes is presented and compared with the measured data.

Strain Distribution in $\text{In}_x\text{Ga}_{1-x}\text{N}$ Disk-in-Wire Superlattice Structure

The detailed description of the InN/InGaN disk-in-wire structure of interest can be found in Ref. 13. Here, we model it by using a superlattice structure along the c -axis, in which each unit cell contains an $\text{In}_x\text{Ga}_{1-x}\text{N}$ quantum disk (QD) with lateral diameter of 29.98 nm and height of 6.24 nm, embedded in a single $\text{In}_{0.4}\text{Ga}_{0.6}\text{N}$ wire as illustrated in Fig. (1). The wire has a hexagonal cross-section with side length of 30 nm and height of 17.75 nm. The geometric parameters are obtained by examining the Transmission Electron Microscopy with High Angle Annular Dark Field (TEM-HAADF) and Energy Dispersive x-ray Spectroscopy (EDS) images in Ref 13. To calculate the strain distribution, we adopt the valence-force field (VFF) model with periodic boundary condition along the z -axis and free boundary condition on the boundary in the $x - y$ plane. Since the VFF model can give a strain tensor at the atomistic level and retain the correct point symmetry of the system, while avoiding potential failure at the interface,¹⁸⁻²⁰ it is chosen in favor of the continuum mechanical model for this work. All the parameters for III-N materials used in VFF model are adopted from Ref. 21, where linear interpolation has been used for the intermediate $\text{In}_x\text{Ga}_{1-x}\text{N}$ alloys. Given the local strain tensor, the strain-induced deformation potential is then incorporated in the EBOM Hamiltonian according to Bir-Pikus theory.²² The strain field influences the electronic states of a InN/InGaN QD via the strain-induced deformation potential and the piezoelectric polarizations. In addition to piezoelectric polarization, due to high electronegativity of nitrogen atom, the spontaneous (pyroelectric) polarization also exists along the c -axis of the WZ crystal.

The strain distribution in $\text{In}_{0.91}\text{Ga}_{0.09}\text{N}$ disk-in-wire structure in the $x - y$ plane and along z -direction are shown in Fig. (2) and Fig. (3), respectively. Figure (4) shows the diagonal elements of the strain Hamiltonian along $[100]$, $[010]$, and $[001]$ directions. Here $V_{ss} = a_2(\epsilon_{xx} + \epsilon_{yy}) + a_1\epsilon_{zz}$, $V_{xx} = l_1\epsilon_{xx} + m_1\epsilon_{yy} + m_2\epsilon_{zz}$, $V_{yy} = m_1\epsilon_{xx} + l_1\epsilon_{yy} + m_2\epsilon_{zz}$, and

$V_{zz} = m_3(\epsilon_{xx} + \epsilon_{yy}) + l_2\epsilon_{zz}$. We see that the hydrostatic strain is approximately uniform throughout the disk, which justifies the divide-and-conquer approach to be discussed in Sec. (3). In addition, the deformation potential profiles show that the strain effects cause an extra contribution to the energy splitting between the $|s\rangle$ state and $|z\rangle$ state, which adds on the splitting between the conduction band and crystal-field split band. Figure (5) shows the potential energy in $x - y$ plane (Fig. (5.a)) and the decomposition of the overall potential energy into a piezoelectric and a pyroelectric components (Fig. (5.b)), which indicates that the built-in electric potential is mainly contributed by piezoelectric effects. In this case, the piezoelectric potential is about nine times larger than the pyroelectric potential. The modifications to the confinement potential by piezoelectric and pyroelectric effects are of the same order of magnitude as the material band offsets.

Electronic States of Single $\text{In}_x\text{Ga}_{1-x}\text{N}$ Disk-in-Wire Structure

Here we describe how to calculate the electronic states of a single $\text{In}_x\text{Ga}_{1-x}\text{N}$ disk-in-wire structure. The model presented in this section will be used to determine the geometric parameters and indium mole fraction in the disk region by fitting the calculated inter-band transition energy with the dominant peak in the photoluminescence (PL) spectrum measured experimentally. The electronic states of QD depend significantly on the strain distribution in III-N system. Using the strain distribution calculated via VFF model as described in the previous section and the deformation potential, we can evaluate the electronic states by EBOM.

Since the lateral size of the disk region is fairly large (~ 30 nm), the quantum confinement effect is more significant along the x-axis than in the $x - y$ plane. If we first neglect the lateral confinement due to finite size, the system can be described by a zero-th order EBOM Hamiltonian, $H^{(0)}$ suitable for describing a quantum well (QW) along the c-axis with the

strain-induced potential $V(x, y, z)$ in each layer replaced by its average value V_0 in the $x - y$ plane. We then include the effect of lateral confinement and the difference in strain-induced potential $\Delta V(x, y, z) = V(x, y, z) - V_0$ as a correction term $H^{(1)}$. The total Hamiltonian then reads

$$H_{tot} = H^{(0)} + H^{(1)}. \quad (1)$$

An eight-band EBOM for WZ crystal¹⁶ is applied to calculate the eigenstates of $H^{(0)}$. All the EBOM parameters used in this work are adopted from Ref 16 for the room-temperature case. The interactions between any two bond-orbitals located in the same material are taken to be the same as those for the bulk. The interaction parameters between two bond-orbitals located in two different materials (i.e. across the heterojunction) are obtained by using the average of the corresponding matrix elements in the two participating bulk materials. The eigenstates of the $H^{(0)}$ matrix for the QW described in EBOM can be solved efficiently with a band-matrix diagonalization program. The resulting eigenstates are denoted by $|n, \mathbf{k}\rangle$, where \mathbf{k} is the wave vector in the $x - y$ plane and n is the label of QW subbands.

To facilitate the calculation, the eigenfunctions of H_{tot} are expanded in terms of the eigenfunctions of $H^{(0)}$, and the lateral confinement effect is described by the truncated-crystal approximation.²³ In this approximation the EBOM envelope function of a QW state in the lateral direction is approximated by a plane wave $e^{i\mathbf{k}\cdot\mathbf{r}}$ subject to suitable boundary conditions. Using the Jacobi-Anger expansion in cylindrical coordinates, we have

$$e^{i\mathbf{k}\cdot\mathbf{r}} = \sum_m (i)^m J_m(k\rho) e^{im(\phi - \phi_k)}. \quad (2)$$

Since the interface between the nanowire and ambient material has a large band offset, it is reasonable to choose a boundary condition such that all lateral wave functions vanish on the interface, which is approximated by a cylindrical surface with radius r_0 . With this hard-wall boundary condition, the allowed values of k are $\alpha_\nu^m = x_\nu^m / r_0$, where x_ν^m are zeros of the Bessel function $J_m(x)$. Thus, the basis states to use for the expansion for eigenstates of H_{tot}

are described by $|n, m, \nu\rangle$ with

$$\langle \rho, \phi | n, m, \nu \rangle = C_\nu^m J_m(\alpha \rho) e^{im\phi}, \quad (3)$$

where $C_\nu^m = 1/\sqrt{\pi r_0^2 J_{m+1}^2(x_\nu^m)}$ is the normalization constant. Each basis function can be related back to the plane waves via the relation $J_m(\alpha \rho) e^{im\phi} = (-i)^m \int \frac{d\phi_k}{2\pi} e^{i\mathbf{k}\cdot\mathbf{r}} e^{im\phi_k}$. Hence, the matrix elements of $H^{(0)}$ in this basis reads

$$\begin{aligned} \langle n', m', \nu' | H^{(0)} | n, m, \nu \rangle &= \sum_{\mathbf{k}} \langle n', m', \nu' | \mathbf{k} \rangle \langle \mathbf{k} | H^{(0)} | \mathbf{k} \rangle \langle \mathbf{k} | n, m, \nu \rangle \\ &= \int k dk \int d\phi_k E_n^{ebom}(k, \phi_k) \delta_{n',n} I_{\nu, \nu'}^{m', m} \frac{J_{m'}(kr_0) J_m(kr_0)}{[k^2 - (\alpha_{\nu'}^{m'})^2][k^2 - (\alpha_\nu^m)^2]} e^{i(m-m')\phi_k}, \end{aligned} \quad (4)$$

where $E_n^{ebom}(\mathbf{k})$ is the QW energy of subband n at lateral momentum \mathbf{k} obtained by EBOM and

$$I_{\nu, \nu'}^{m', m} = \frac{1}{1} (-1)^{\nu'+\nu+m} (i)^{m'+m} \alpha_{\nu'}^{m'} \alpha_\nu^m. \quad (5)$$

For the $H^{(1)}$ term, which consists of only the potential part, the matrix elements can be written as

$$\langle n', m', \nu' | H^{(1)} | n, m, \nu \rangle = \int f_{n', m', \nu'}^*(z) f_{n, m, \nu}(z) \Delta V_{\nu', \nu}^{m', m}(z) dz, \quad (6)$$

where $f_{n, m, \nu}(z)$ denotes the envelope function of QW along z axis, which is related to the eigenvectors of QW for the n -th subband at $k = \alpha_\nu^m$ obtained from the eight-band EBOM and averaged over angle. We have used the root-mean-square value of bond-orbital coefficients on each site to get a smooth envelope function.

$$\Delta V_{\nu', \nu}^{m', m}(z) = \int_0^{2\pi} \int_0^{r_0} C_{\nu'}^{m'} C_\nu^m J_{m'}(\alpha_{\nu'}^m \rho) J_m(\alpha_\nu^m \rho) \Delta V(\rho, \phi, z) \rho d\rho d\phi. \quad (7)$$

In this manner, the electronic states in $\text{In}_x\text{Ga}_{1-x}\text{N}$ disk-in-wire can be solved efficiently in the subspace of the full Hamiltonian defined by the selected subband states obtained from EBOM.

Determination of Indium Mole Fraction in Disk Region

In this section, we perform the calculation of electronic state of single $\text{In}_x\text{Ga}_{1-x}\text{N}/\text{In}_{0.4}\text{Ga}_{0.6}\text{N}$ disk-in-wire structures, which is presented in Sec. (3), in order to determine the indium mole fraction at disk region by fitting the energy of the dominant PL peak. Figure (6) shows the subband structures of a 6.24 nm-wide $\text{In}_{0.91}\text{Ga}_{0.09}\text{N}$ disk in the lateral direction. Note that the top four valence bands are doubly degenerate at the zone center which corresponds to the heavy-hole and light-hole bands, while the single-fold states correspond to the split bands due to the crystal field. The crystal-field split bands are pushed down in energy due to the deformation potential contributed from the strain. Figure (7) shows the band profile in the growth direction as well as the calculated electronic states in an $\text{In}_{0.91}\text{Ga}_{0.09}\text{N}$ QW structure. The dominant PL peak measured at 300 K occurs at 0.7485 eV (z -direction) +0.0075 eV (lateral direction) = 0.7560 eV and the best-fit indium composition inside the active region of the disk is $\sim 91\%$.

Carrier Leaking Rate in Quantum Well System: Multi-Band Transfer-Matrix Method

In order to study the photocurrent spectra, we calculate the leaking rate of a carrier in the full epitaxial structure of the device. There are multiple theoretical methods for evaluating the carrier tunneling rate, including the phase-shift method,²⁴ the complex-energy method,²⁵ and the stabilization method.^{26,27} The main drawback for both the phase-shift method and the complex-energy method is the requirement of accurate description of wavefunctions. In contrast, the stabilization method requires only the eigenvalues of the system Hamiltonian as functions of an external parameter, such as the size of simulation domain. It can calculate the electron/hole leaking rate (or carrier lifetime) given the actual coupling strength between states, and the width of the generated DOS averaged by a scaling parameter. However, it is

impractical when the device has a complicated structures and possesses multiple tunneling channels. Besides that, the stabilization method cannot really incorporate the continuum-to-continuum state transitions. As a result, we adopt an approach which is based on transfer-matrix method (TMM) to calculate the reflection coefficient spectra of the InN/InGaN disk-in-wire photodiode, and relate that to the leaking rate of bound or quasi-bound states in the disk region. Again, the band structure information is incorporated via an eight-band EBOM, while suitable boundary conditions are applied at the contact region (or the boundary of the simulation domain).

A numerically stable version of multi-band TMM base on EBOM for the devices composed of ZB semiconductor can be found in Ref 28, which can be easily extended into the system with WZ materials. Here, we set up the transfer-matrix equations for WZ material, and solve the resulting linear equation by using a band matrix solver. The reflection coefficients obtained from the TMM can be used to determine the leaking rate for the bound or quasi-bound states in the active region, which quantitatively describe the carrier tunneling in the active region through the barrier. The leaking rate so determined is utilized in the calculation of the photocurrent strength of InN/InGaN disk-in-wire photodiode.

The idea of using reflection coefficients to describe the leaking rate (or tunneling rate) of carriers in the active region is rather simple. In the TMM model, an incident wave from the contact serves as the input of the calculation. Normally, we assign the amplitude of the incident wave to be one at a certain available channel which is determined from the complex-band structure²⁹ (including real k solution for the propagating waves along the carrier-transport direction and complex k for evanescent waves). In this manner, the amplitude reflected and transmitted can be easily calculated by comparing with the amplitude of the assigned incident wave. If the system is composed of non-absorbing material, the sum of the transmission and reflection coefficient is one. If there is a finite absorption in the system, the incident wave is absorbed by the material with an amount proportional to the probability of the electron being inside the bounding area. In this work, we artificially introduce a small

damping in the system, and a sharp dip appears in the reflection spectra due to the fact that the energy of incident wave matches that of a bound or quasi-bound state. The incident wave can be viewed as a probe, which excites a bound state when their energies match, and that leads to a strong absorption due to the relatively large magnitude of the bound state in the active region. As for the incident waves with energies which do not match any bound states or quasi-bound states, these incident waves bounce back with almost full magnitude and contribute relatively large reflection coefficients in the reflectance spectra. This method allows us to localize the energies of bound states (or quasi-bound state, depending upon the ratio of the wave function amplitude across the interface between the barrier and active region). At the same time, the actual wavefunction can be generated from the TMM. Note that the artificial damping parameter, γ introduces energy broadening in the energy spectra. The value of γ is inversely proportional to the carrier lifetime. Therefore, the γ cannot be larger than the actual energy broadening observed in the experimental spectra. For illustration, we show the calculated reflection spectra of an InN/InGaN multi-QW structure for both the quasi-bound states and the non-resonance states in Fig. (8). Fig. (8a,b) shows the case when the selected energies are in resonance with quasi-bound states, while Fig. (8c,d) shows the case when the selected energies are out of resonance. The relative strength of leaking rates are assumed proportional to the depths of the dips.

Determination of Band Bending and Dominant Photon Absorption Process

In this section, we perform the TMM simulation, which is described in Sec. (5), to calculate the leaking rate spectra considering the full InN/InGaN disk-in-wire photodiode and determine the dominant photon absorption process for the photocurrent. Given the indium mole fraction in the disk region, strain-induced deformation potential, and the polarization field obtained from single disk-in-wire calculation, the full-device structure can be built up

by repeating the potential profile of the single disk-in-wire structure four times to account for four disks in one nanowire structure, and sandwiching it between graded-index p- and n-doped layers according to the epitaxial structure in Ref. 13. To incorporate the electric field contributed from both the external bias and the built-in potential of the p-i-n structure, we use the self-consistent transport model based on non-equilibrium Green's function (NEGF) to estimate the band-bending effect induced from both carrier injection and doping concentration. Figure (9) shows both the flat-band diagram (Fig. (9.a)) and the band diagram under non-equilibrium conditions (Fig. (9.b)). Due to the unintentionally n-doping, the central intrinsic region is assumed to have a n-type concentration of $7.5 \times 10^{-16} \text{ cm}^{-3}$. This unintentionally n-doped concentration is of importance since it influences not only the band diagram in the active region, but also the relative band bending between the active region and contact, that further affects the tunneling behavior of carriers.

Given the self-consistent potential under non-equilibrium condition including the spatially dependent doping profile, the leaking-rate spectra can be calculated using EBOM-based TMM. We start with the leaking-rate spectra of the $\text{In}_{0.91}\text{Ga}_{0.08}\text{N}/\text{In}_{0.4}\text{Ga}_{0.6}\text{N}$ disk-in-wire guided wave photodiode at the zone center ($k_x = k_y = 0$), which is shown in Fig. (10.a). Figures (10.b) and (10.c) show the first three quasi-bound states corresponding to the first three dips in the leaking-rate spectra (Fig. (10.a)), the first hole bound states, as well as the electronic bound states at each QW region. By examining the energy separations between bound states and quasi-bound states, one can determine the possible photon absorption process in such structure.

There are typically three major mechanisms which contribute to the photocurrent, and one can roughly distinguish them by examining the energy separation and photocurrent peak positions. The first one is the simple one-photon absorption process, in which the electron transits into a quasi-bound state in the conduction band and contributes to photocurrent via the direct tunneling process. In this case, the photocurrent peak positions are determined by the SPA spectra multiplied by tunneling rate of each quasi-bound state. The second

mechanism is photoabsorption followed by phonon-assisted tunneling. Namely, carriers in the confined region jump to an excited state via photoabsorption, then escape from the active region by absorbing phonons. In this case, the energy separation between the initial and final states should match the photon energy plus the energy of available phonon in the material, and the photocurrent peak positions are determined by the single-photon absorption (SPA) process involving a bound state and an excited state below the tunneling threshold by a phonon energy. The third mechanism is two-photon absorption (TPA) process. The carrier is initially in the valence band or conduction band, and jump into quasi-bound states by absorbing two photons. In this case, both photons involved in the TPA process have identical energy, and the photocurrent peak position is determined by the single photon energy.

We first look into the SPA process. The minimum possible SPA energy is the transition involving the first quasi-bound level in conduction band and top level in valence band. From Fig (10.c), the separation between these two states is $2.1152 - 0.4312 = 1.6840$ eV, which is much larger than the first measured photocurrent peak, which is around 1 eV. Even with the phonon-assisted photoabsorption, the threshold for photocurrent can only be lowered by the available phonon energy, which is close to 26 meV at room temperature for the experimental condition considered here. As a result, the dominant absorption process which contributes to the photocurrent below 1.7 eV is mainly caused by the TPA, although SPA still contributes to photocurrent at the higher energy region. Thus, both the SPA and TPA need to be considered in this work for calculating the photocurrent spectra generated by $\text{In}_{0.91}\text{Ga}_{0.09}\text{N}$ disk-in-wire photodiode.

One-Photon and Two-Photon Absorption

The optical properties of interest include both the inter-band transition and intra-band transition. Here we briefly describe the derivation for the momentum dependent optical matrix elements from the EBOM Hamiltonian. The detailed derivation for the case of ZB

material was reported in Ref. 15. We extend the derivation by using the EBOM Hamiltonian suitable for WZ materials.¹⁶

The optical matrix elements between EBOM basis ($|s\rangle$, $|x\rangle$, $|y\rangle$, and $|z\rangle$) is given by

$$\frac{\hbar}{m_0} \langle \alpha', \mathbf{k} | \hat{\beta} \cdot \mathbf{p} | \alpha, \mathbf{k} \rangle = i \langle \alpha', \mathbf{k} | \hat{\beta} \cdot [H, \vec{\rho}] | \alpha, \mathbf{k} \rangle = i \langle \alpha', \mathbf{k} | \hat{\beta} \cdot [H_{ebom}^{8 \times 8}, \vec{\rho}] | \alpha, \mathbf{k} \rangle. \quad (8)$$

where the unit vector $\hat{\beta}$ represents the polarization of the incident light. In reciprocal space, we can write the position vector $\vec{\rho}$ as an operator $i\nabla_{\mathbf{k}}$, and hence we have

$$[H_{ebom}^{8 \times 8}, \vec{\rho}] = -i\nabla_{\mathbf{k}} H_{ebom}^{8 \times 8}(\mathbf{k}), \quad (9)$$

which leads to a simple analytic expression suitable for \mathbf{k} in the full BZ,

$$P_{\beta}^{\alpha, \alpha'}(\mathbf{k}) = \hat{\beta} \cdot \nabla_{\mathbf{k}} H_{ebom}^{8 \times 8}(\mathbf{k}). \quad (10)$$

Note that Eq. (10) can be used for the calculation of both inter-band transition and intra-band transition.

Given the optical matrix elements, we can investigate the optical properties of $\text{In}_x\text{Ga}_{1-x}\text{N}$ QW through the dielectric function $\epsilon \equiv \epsilon_1 + i\epsilon_2$. The imaginary part ϵ_2 for the polarization is given by³⁰

$$\begin{aligned} \epsilon_2(\omega) &= \frac{2\pi e^2}{V\omega^2} \sum_{k_{||}; i, j} |\langle \mathbf{k}_{||}, i | P_{\beta} | \mathbf{k}_{||}, j \rangle|^2 \delta(E_j(\mathbf{k}_{||}) - E_i(\mathbf{k}_{||}) - \hbar\omega) \\ &= \frac{e^2}{2\pi d\omega^2} \sum_{i, j} \int d^2k_{||} |\langle \mathbf{k}_{||}, i | P_{\beta} | \mathbf{k}_{||}, j \rangle|^2 \delta(E_j(\mathbf{k}_{||}) - E_i(\mathbf{k}_{||}) - \hbar\omega) \end{aligned}, \quad (11)$$

where $|\mathbf{k}_{||}, i\rangle$ denotes the i th electronic state of the quantum well associated with wave vector $\mathbf{k}_{||}$, $\hbar\omega$ denotes the photon energy, and V denotes the volume of the slab, which can be written as the cross-sectional area multiplied by the slab thickness. Due to the translational invariance in the lateral direction (x, y), the summation over $\mathbf{k}_{||}$ is replace by

integral $A/4\pi^2 \int d^2k_{\parallel}$. The real part of the dielectric function (ϵ_1) can be obtained from the imaginary part (ϵ_2) by utilizing the Kramers-Kronig relation. The one-photon absorption coefficient is related to $\epsilon_2(\hbar\omega)$ by

$$\alpha(\hbar\omega) = \frac{\omega}{cn_r} \epsilon_2(\hbar\omega), \quad (12)$$

where c is the speed of light, n_r is the refractive index of the active material.

The TPA coefficient (β_2) for the QW is given by³¹

$$\beta_2 = \frac{8\pi\omega}{c^2\epsilon_1(\omega)V} \sum_{\mathbf{k}_{\parallel}, mn} |M_{mn}(\mathbf{k}_{\parallel})|^2 \times \delta[2\hbar\omega - E_n(\mathbf{k}_{\parallel}) + E_m(\mathbf{k}_{\parallel})], \quad (13)$$

where

$$M_{mn}(\mathbf{k}_{\parallel}) = 2\left(\frac{e}{m_e\omega}\right)^2 \sum_s \frac{\langle n\mathbf{k}_{\parallel} | \hat{\epsilon} \cdot \mathbf{p} | s\mathbf{k}_{\parallel} \rangle \langle s\mathbf{k}_{\parallel} | \hat{\epsilon} \cdot \mathbf{p} | m\mathbf{k}_{\parallel} \rangle}{\hbar\omega - [E_s(\mathbf{k}_{\parallel}) - E_m(\mathbf{k}_{\parallel})] + i\Gamma}. \quad (14)$$

$E_m(\mathbf{k}_{\parallel})$, $E_s(\mathbf{k}_{\parallel})$, and $E_n(\mathbf{k}_{\parallel})$ denote the energies of initial, intermediate, and final state, respectively. The intermediate states, $|s\mathbf{k}_{\parallel}\rangle$, can be either conduction or valence subband states. For all transitions, the initial state must be occupied and the final state must be empty. For simplicity, we have not included the effect of thermal excitation, although it is not negligible at room temperature. Such an effect will be left for future research. To avoid the singularity coming from the denominator of the second-order perturbation theory, an imaginary number ($i\Gamma$) is introduced in Eq. (14). The linewidth parameter Γ is related to the finite lifetime of the QW states. All the optical constants for III-N materials used in this work are adopted from Ref 32.

In order to capture all possible transitions in the device, all the states corresponding to different \mathbf{k}_{\parallel} 's are needed in the calculation of absorption. For WZ materials, both the band structure and optical matrix elements have strong anisotropy. As a result, the \mathbf{k}_{\parallel} integration cannot be avoided in this case. There are several ways to conduct the \mathbf{k}_{\parallel} integration, including the method of selecting a special \mathbf{k} point with proper weighting according to the

symmetry of crystal,³³ or simply doing a dense-mesh zone integration in the desired portion of first BZ. In this work, we apply the zone-integration method with area-dependent weighting to capture the full transition characteristics in the first BZ. Due to the C_3 symmetry of WZ crystal, we only sample \mathbf{k}_{\parallel} within the triangle with vertices at Γ , K , and M points as shown in Fig (11).

The other effect introduced by the lateral confinement is the energy quantization in the transverse direction. In the disk-in-wire system, both the interface defined by the high-indium QD and the nanowire structure impact confinement. For the InGaN QD interface, the quantum confinement, the deformation potential induced by strain, piezoelectric field, and the material band offset have been taken into account in our model calculation. Again, due to the fairly large wire structure in our system (radius = $26nm$), the confinement effect is expected to be small, and the distribution of available \mathbf{k}_{\parallel} states in reciprocal space can be approximated by a continuum. However, in the low energy region, where the spacing between available \mathbf{k}_{\parallel} states are relatively large, and the energy quantization still makes a noticeable modification to the absorption spectra.

In Fig. (12.a), we show the distribution of allowed \mathbf{k}_{\parallel} 's which satisfy the boundary condition $J_n(kr_0) = 0$ for a nanowire structure with radius $r_0 = 26.053$ nm based on the truncated-crystal approximation. In this work, we first generate a DOS curve defined by $D(k_{\rho}) = \sum_{\mathbf{k}_{\parallel}} \delta(k_{\rho} - k_{\parallel})$ as a function of the magnitude of k_{ρ} by introducing a broadening in the delta functions (Fig. (12.b)). We then use interpolation to obtain the weighting factor that accounts for the DOS due to lateral confinement at each sampling point of \mathbf{k}_{\parallel} as shown by the black dots in Fig. (11.b). Due to large spacings among allowed states in the low energy region, the weighting factor that reflects the correction due to lateral confinement is relatively strong near the zone center. To summarize, we have introduced two weighting factors: one accounts for the zone integration effect and the other accounts for the energy squeezing effect induced by lateral confinement.

Photon Density-of-States in a Graded-Index Waveguide

The graded-index layers of the epitaxial design in the considered InN/InGaN disk-in-wire photodiode only allows photons with certain energies to propagate in the layer of nanowire arrays. The peaks of the photocurrent spectra occur when the photon is in resonance with cavity modes, and the absorption strength at those resonance energies is significant, which indicates good electron-photon coupling in the active region. As a result, the DOS of optical waves propagating in the photodiode can also influence the peak positions in the photocurrent spectra.

The considered graded-index waveguide structure and the corresponding refractive index of each layer at ~ 1 eV are shown in Fig. (13.a) and Fig. (13.b), respectively. It consists of n-/p-doped $\text{In}_x\text{Ga}_{1-x}\text{N}$ graded-index layer with $x = 0.4 \sim 0.04$, and disk-in-wire array at the center as the active layer. The entire graded-index structure is sandwiched by p-/n-doped GaN cladding layers. A thick silicon substrate layer and an air layer are also incorporated in our simulation in order to capture the accurate dispersion curves for both the guided mode and resonance mode. In our simulation, a three-dimensional structure consisting of two-dimensional disk-in-wire array with wire width = 60 nm and fill factor of 0.91 is considered. The photonic band structure of the $\text{In}_{0.91}\text{Ga}_{0.09}\text{N}/\text{In}_{0.4}\text{Ga}_{0.6}\text{N}$ disk-in-wire photodiode inside a graded-index waveguide structure is calculated based on the RCWA method. Since the dielectric constants of materials involved are functions of the photon energy, the input photon energy is scanned for the solution of k_x that satisfies the Maxwell's Equations. The results are shown in Fig (14) for both TE (y -polarization) and TM (z -polarization) modes. Each point in Fig. (14) corresponds to a propagating mode in the $\text{In}_{0.91}\text{Ga}_{0.09}\text{N}/\text{In}_{0.4}\text{Ga}_{0.6}\text{N}$ disk-in-wire waveguide with a certain propagation constant (k_x). The shadow in the background corresponds to the intrinsic modes in constituent bulk materials including the silicon substrate and air (slab mode). The heavy dark curves describe the dispersion of the guided wave associated with the graded-index structure. The dispersion curves have a finite width since they can still leak into the substrate. The width

of the dispersion curves in the high-energy region becomes narrower as they represent the well-confined modes in the device. In regions where the dispersion curves are broadened, the photon modes are more leaky, which are identified as resonance modes. If the silicon substrate is removed in the simulation, the typical guided mode dispersion curves above the air light line become clear sharp lines, while the continuum modes, which correspond to the radiation modes, appear below the air light line.

It is noted that for confined modes the photon with small propagation constant (below air light line) tend to have relatively large DOS due to the small slope (dE/dk_x) of the dispersion curve near zone-center, especially for TM modes.³⁴ As a result, the optical transition process are more involving with the less-confined modes near $k_x = 0$ than the well-confined modes above the air light line. In our case, since the fill factor of the disk-in-wire array is fairly large (~ 0.91), the modal dispersion curves below the air light line are difficult to distinguish from the slab modes. However, confined modes in this region with small group velocity along the x -axis still exist in the present structure. To help sort out the characteristics of the resonance modes, the probability distribution of each mode is calculated in each region of the device structure and show their modal density in the nanowire layer for TE and TM modes in Fig. (15). By comparing Fig. (15.a) and (15.b), the TM modes show over-all stronger modal density in the nanowire array region. As a result, we expect the effect of the photon DOS is mainly contributed by TM modes, and only TE modes with cut-off energy near 0.95 eV and 1.6 eV have comparable modal density with those of TM modes. However, since the absorption above ~ 1 eV is dominated by TM modes (which will be discussed in the next section), we only include the TE-mode contributions with cut-off energies near 1 eV in the photocurrent calculation. Based on the discussion above, we shall quantitatively characterize the effect of the photon DOS by the segments of dispersion curves below the air light line. The photon DOS for each resonance mode are fitted with the Lorentzian functions with the center of functions corresponding to the cut-off energy and the broadening width determined by the spread of each group of dispersion curves near $k_x = 0$. From Fig. (15.b),

we determine the cut-off energies of the TM modes that are of interest as 1.03 eV, 1.38 eV, 1.62 eV, and 2.06 eV, while the corresponding broadening widths are 0.4 eV, 0.9 eV, 0.4 eV, and 1.7 eV, respectively. The TE mode with 0.95 eV cut-off energy and = 0.4 eV broadening width is also included (Fig. (15.a)). The fundamental mode and first excited mode for both TE and TM polarizations are not selected due to their poor modal density with TPA absorption spectra. Note that both TE and TM resonance modes with cut-off energy near ~ 1 eV exist in the photonic band structure of the waveguide. As a result, the DOS near 1 eV, which consists of two Lorentzian functions attributed to TE and TM components, is about twice as strong compared to others in this work.

Results and Discussions

In this section, we discuss how to combine the carrier tunneling rate with the absorption spectra to get the photocurrent spectra. A selection of 55 sampling points are chosen for the wave vector \mathbf{k}_{\parallel} within $1/12$ of the first BZ as illustrated by dark dots in Fig. (11.b). The reflection spectra is then calculated at each sampling \mathbf{k}_{\parallel} by using EBOM-based TMM described in Sec. (5). In Fig. (16), we show the reflection spectra with the damping parameter $\gamma = 10$ meV for various sampling wave vectors. Each dip in the reflection spectra reflects significant absorption at that energy, indicating the existence of quasi-bound or bound state. The energies and wavefunctions corresponding to these dips are then collected and a set of quasi-bound states is constructed, which serve as available tunneling channels for carriers to reach the contact. The relative strengths of leaking rates are assumed proportional to the depths of the dips. As for the calculation of absorption spectra, since the experiment was conducted with the light incident from the $y - z$ facet, only the absorption corresponding to y -polarized and z -polarized photons is considered. By multiplying the leaking rate of a tunneling state and the absorption coefficient for a transition into that state, the contribution from that transition to the photocurrent spectrum is obtained. Integrating all these

transitions over the sampling points in \mathbf{k}_{\parallel} gives rise to the total photocurrent spectrum.

Figure (17) shows the photocurrent spectrum due to SPA for the $\text{In}_{0.91}\text{Ga}_{0.09}\text{N}$ disk-in-wire structure. The whole spectrum is broadened with $\sigma = 0.1$ eV due to the inhomogeneity of the structure. As expected, the first absorption peak appears in the energy region higher than 1.5 eV. This suggests that the measured photocurrent peaks in low-energy region are attributed to some mechanisms other than SPA. The SPA absorption mainly contributes to the photocurrent around 2 eV, where the dominant SPA process is due to the y -polarized photon.

The TPA processes can be categorized into two different types depending upon the selection of the intermediate state: VB-CB-CB, which uses conduction subband states as intermediate states, while VB-VB-CB uses valence subband states as intermediate states. Figure (18) shows the photocurrent spectra via VB-CB-CB absorption of the $\text{In}_{0.91}\text{Ga}_{0.09}\text{N}$ disk-in-wire structure. The calculated spectra show a three-packet feature for both y - and z -polarized photons with z -polarization about 10 times stronger than the y -polarization. Figure (19) shows the photocurrent spectra induced by VB-VB-CB type transition. It is seen that VB-VB-CB is generally stronger than VB-CB-CB in the low-energy region due to a higher DOS for the valence subbands. The photocurrent strengths for y -polarization and z -polarization are closer for VB-VB-CB transitions with the y -polarization strength about 2.5 times stronger. Note that the first and second packets due to VB-CB-CB transitions and the packet below 1 eV due to VB-VB-CB transitions do not really satisfy the double-resonance condition of TPA, but they are enhanced significantly by the ω^{-3} factor in Eq. (11). This implies that the photocurrent peaks in the low energy region are pinned and less sensitive to external bias. From Figs. (18) and (19), we expect that the photocurrent spectra in the region between 1.2 eV and 2.5 eV are mainly contributed by the VB-CB-CB transitions, while VB-VB-CB transitions are dominant in the low energy region (< 1 eV).

Figures (20.a) and (20.b) show the calculated total photocurrent spectra (red line) at -1 V bias with and without considering the photon DOS, respectively, as well as their

comparison with the experimental data (blue line). Note that in order to compare the calculated photocurrent spectra with experimental data, the energy dependence of the intensity distribution of the light source, the response of detector, and the grating efficiency must be included in the calculation. Those functions adopted from equipment specifications are shown in Fig. (20.c), and they are incorporated in the calculation. In the case without considering the effect of the photon DOS (Fig (20.a)), the peak positions in the calculated spectra match the weak features observed experimentally. The calculated photocurrent spectra shows peaks at 0.806 eV, 1.287 eV, 1.914 eV, 2.009 eV, and 2.405 eV. The first peak corresponds to TPA with VB-VB-CB transition. The second and last peak correspond to TPA with VB-VB-CB transitions, while peaks around 2 eV are induced by SPA. In the measured photocurrent spectra under the -0.1 V bias, there are two peaks near 0.8 eV and 1 eV, while the one near 0.8 eV is less noticeable under -1 V external bias due to relatively large broadening.

After including the effect of the photon DOS, optical transitions with energies matching the photon DOS peaks in the cavity are greatly enhanced, leading to additional peaks, which can mask the original peaks. As a result, the three packets of peaks in the calculated photocurrent spectrum appear blue shifted, and they are in much better agreement with experimental results at -1 V bias. The first peak is shifted to 0.95 eV and the peak originally at 0.806 eV in the case without photon DOS correction becomes a small shoulder of the first packet which is also seen in the measured data with external bias = -0.1 V. The peak originally at 1.287 eV in the case without photon DOS correction becomes a shoulder of the second packet, while another peak appears at 1.38 eV. Besides that, a peak appears at 1.62 eV after considering the photon DOS. However, due to the small absorption strength in the range from 1.5 eV to 1.8 eV, this peak merges into the second packet which is consistent with the experimental data. The second last peak at 2.039 eV corresponds to VB-CB-CB transition peak at 2.066 eV coupled with z-polarized photon. The very last peak at 2.375 eV corresponds to the non-coupling peak at 2.296 eV with VB-CB-CB TPA transition in

the measured photocurrent spectra. A peak corresponding to SPA is also present at 1.91 eV in the calculated spectra. We note that the deviations of the lineshape between the calculated spectrum and the measured data between 1.2 eV and 1.9 eV are attributed to our approximation of the photon DOS by using a few Lorentzian functions. It may be improved by incorporating the actual photon DOS calculated from the dispersion curve of resonance modes. Furthermore, the ratio of strengths between SPA and TPA used in the calculation is uncertain, since it depends on light intensity inside the active region, which cannot be determined accurately.

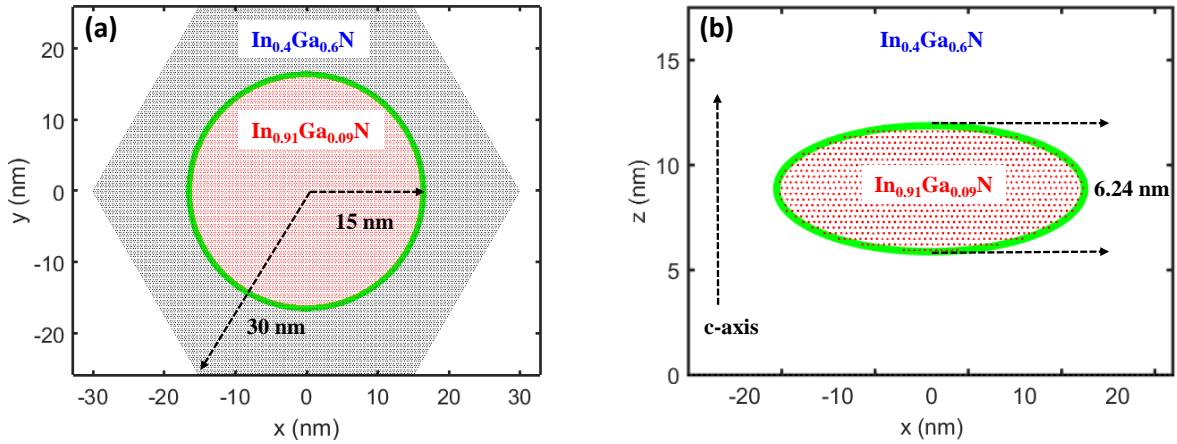


Figure 1: (a) Schematic diagram of a cross-section in the $x - y$ plane for $\text{In}_x\text{Ga}_{1-x}\text{N}$ disk buried in $\text{In}_{0.4}\text{Ga}_{0.6}\text{N}$ structure. (b) The side view of the same structure.

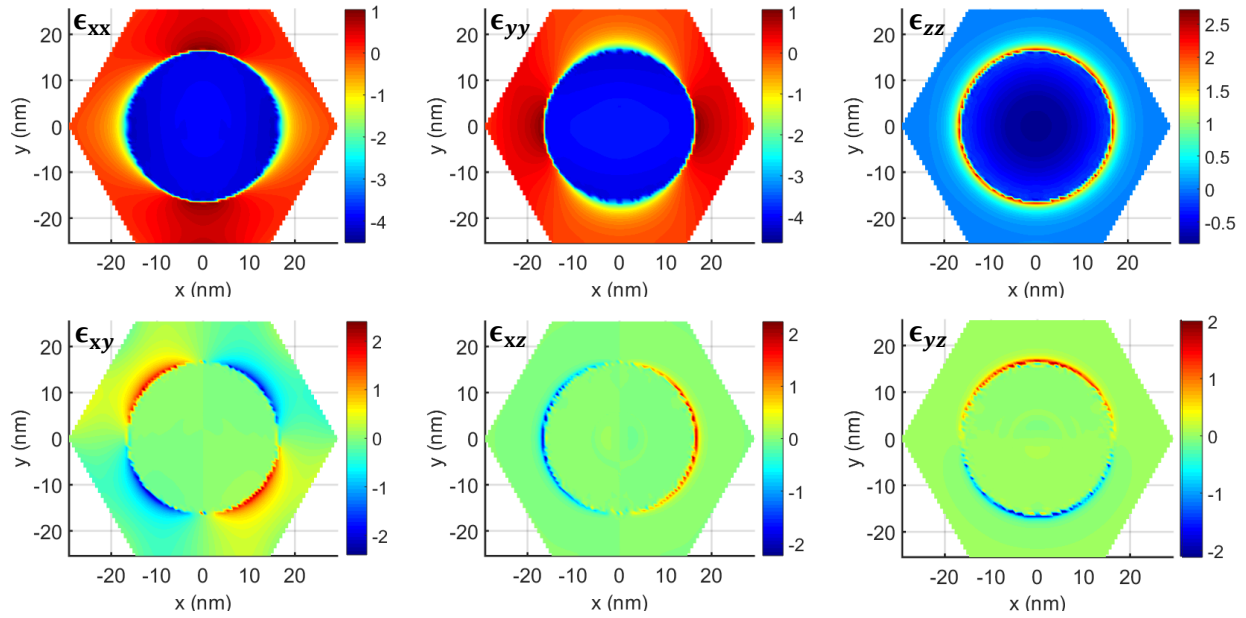


Figure 2: Calculated strain distribution in an $\text{In}_{0.91}\text{Ga}_{0.09}\text{N}$ disk with 6.24 nm height in the plane passing through the center of the disk ($z = 8.64$ nm). The unit are in percentage.

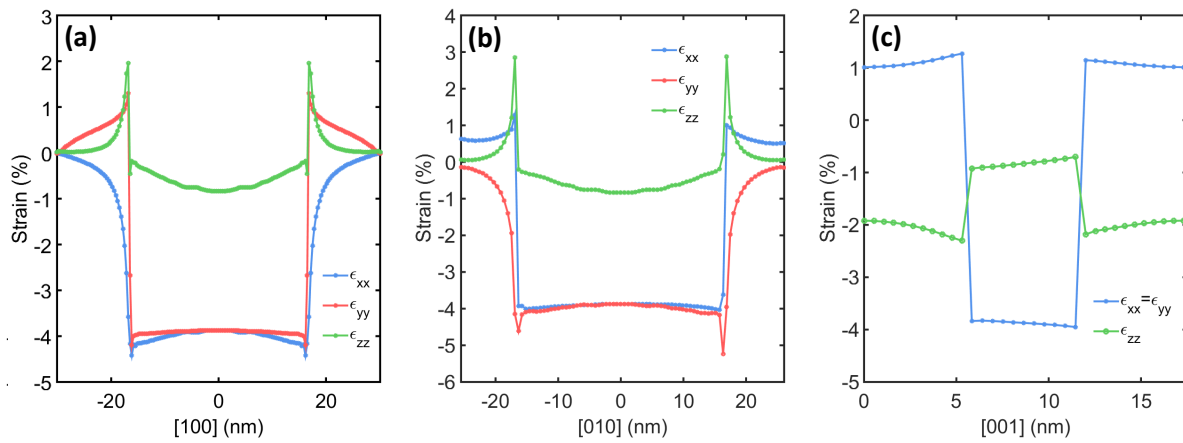


Figure 3: Calculated strain distribution in an $\text{In}_{0.91}\text{Ga}_{0.09}\text{N}$ dot with 6.24 nm height along a line passing through the center of the disk and parallel to (a) x axis, (b) y axis, and (c) z-axis.

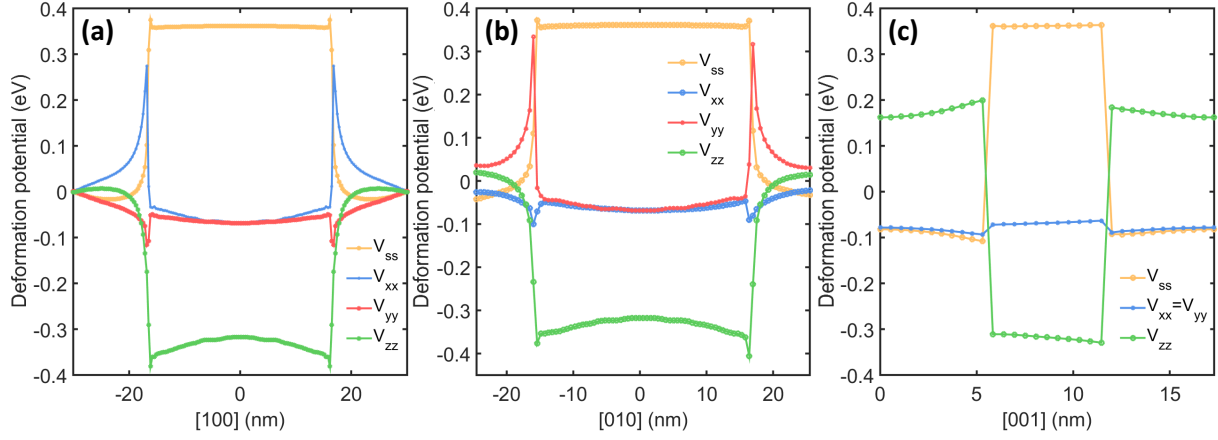


Figure 4: Diagonal elements of the deformation potential for $\text{In}_{0.91}\text{Ga}_{0.09}\text{N}$ disk with 6.24 nm height along a line passing through the center of the disk and parallel to (a) x axis, (b) y axis, and (c) z-axis.

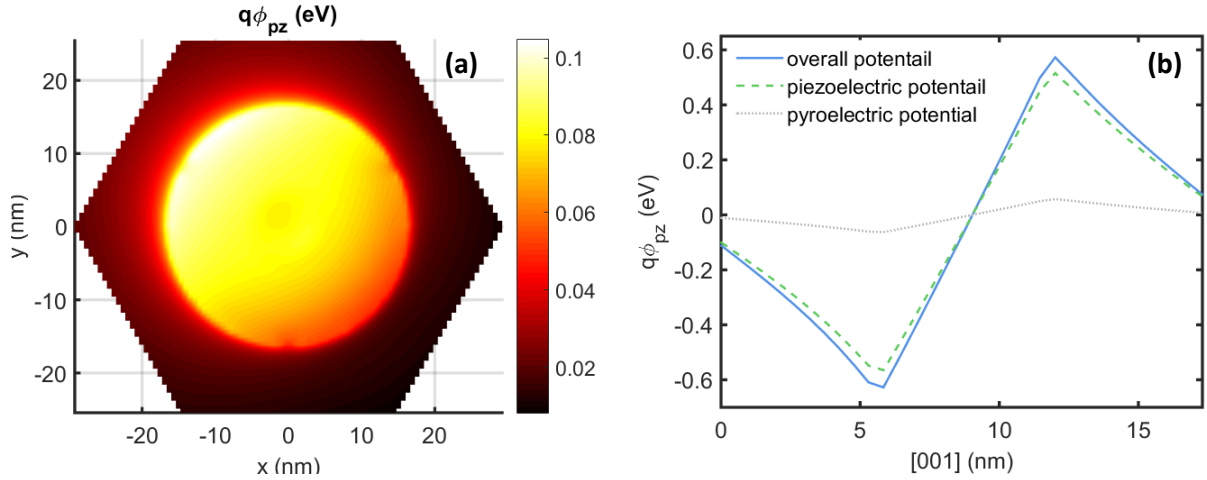


Figure 5: Calculated built-in electric potential in an $\text{In}_{0.91}\text{Ga}_{0.09}\text{N}$ disk with 6.24 nm height. (a) The overall electric potential map in the plane of $z = 8.64$ nm. (b) The linescan of the built-in potential along the [0001] direction through the disk's center. The solid line shows the overall potential, and the dashed line and the dotted line show the components induced by the piezoelectric polarization and the pyroelectric polarization.

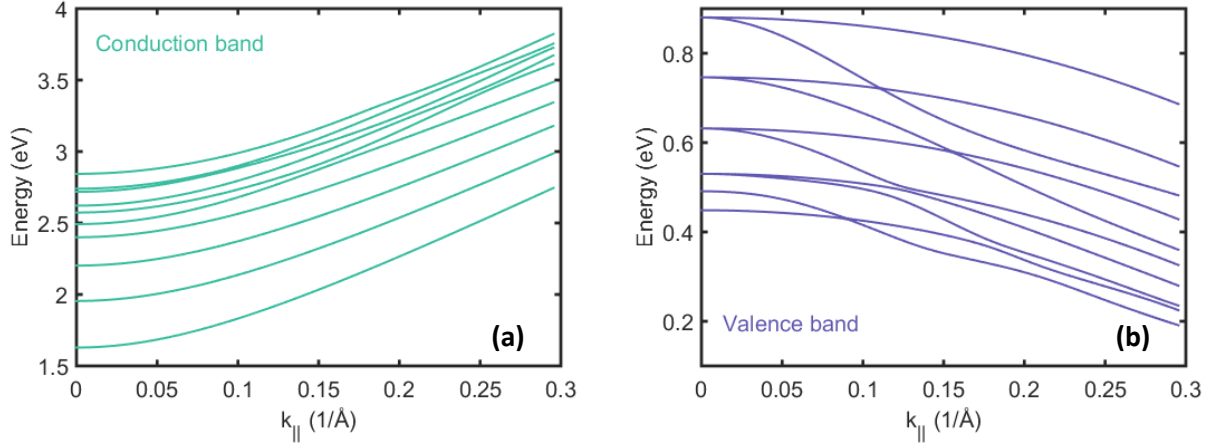


Figure 6: Subband structures of a 6.24 nm width $\text{In}_{0.91}\text{Ga}_{0.09}\text{N}$ QW for an electron in (a) conduction band and (b) valence band.

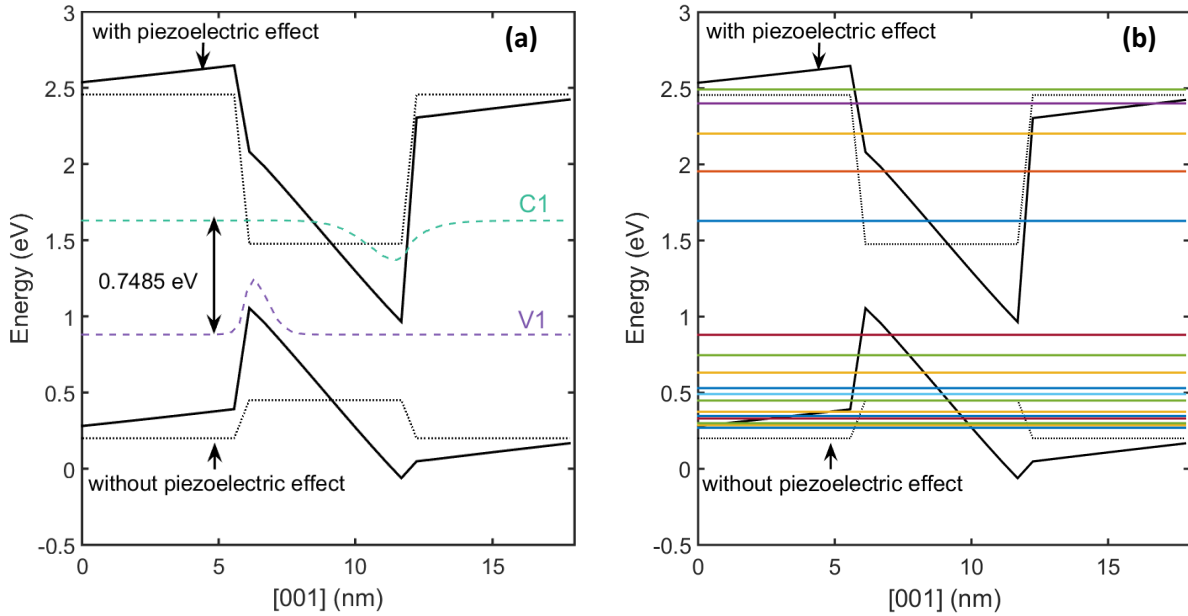


Figure 7: The in-plane averaged band profile for an $\text{In}_{0.91}\text{Ga}_{0.09}\text{N}$ quantum well structure with 6.24 nm width with (solid line) and without (dotted line) piezoelectric effect. (a) The corresponding ground state in conduction and valence band (dashed lines). (b) The bottom 5 energy levels in the conduction band and top 20 energy levels in the valence band (colored lines).

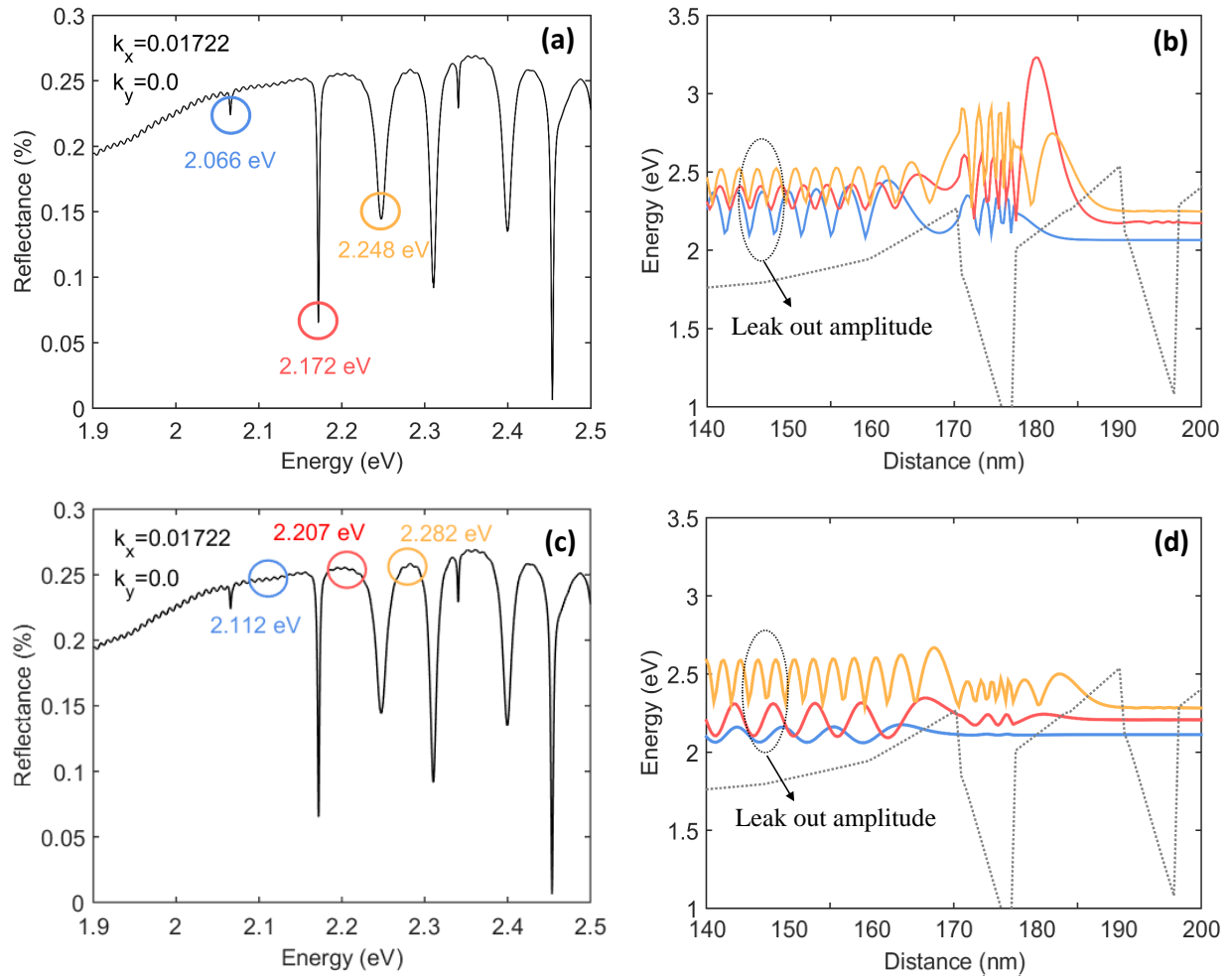


Figure 8: Reflection spectra and wave functions of quasi-bound states for InN/InGaN multi-QW structure calculated by EBOM-based TMM. (a) Reflection spectra with positions of quasi-bound states indicated by circles. (b) Wave functions of quasi-bound states with energies positions indicated by circles in (a). (c) Reflection spectra with a few selected non-resonant energy positions indicated by circles. (d) Wave functions of non-resonant states with energies positions indicated by circles in (c).

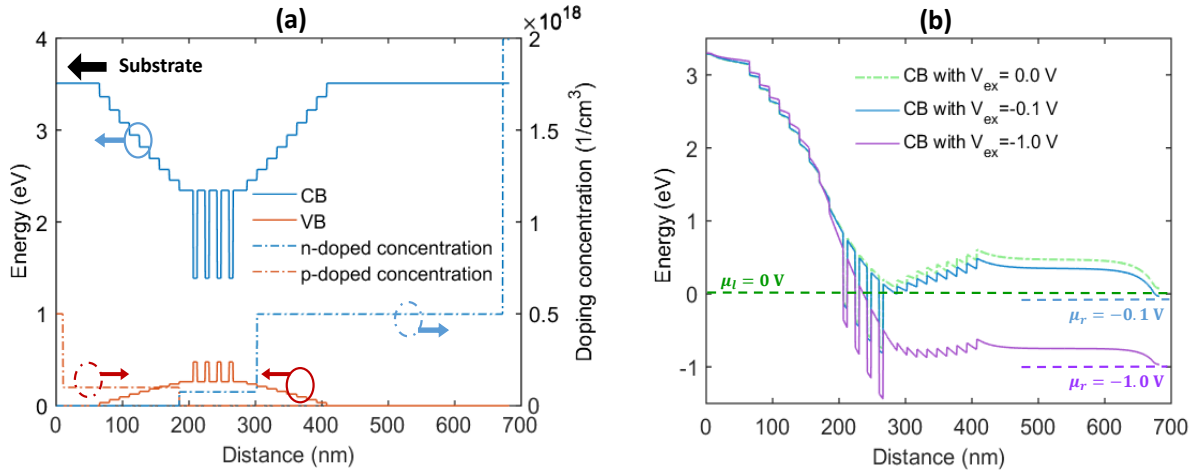


Figure 9: (a) Flat-band diagram for InGaN photodiode. (b) Self-consistent band diagram under various external bias calculated by NEGF.

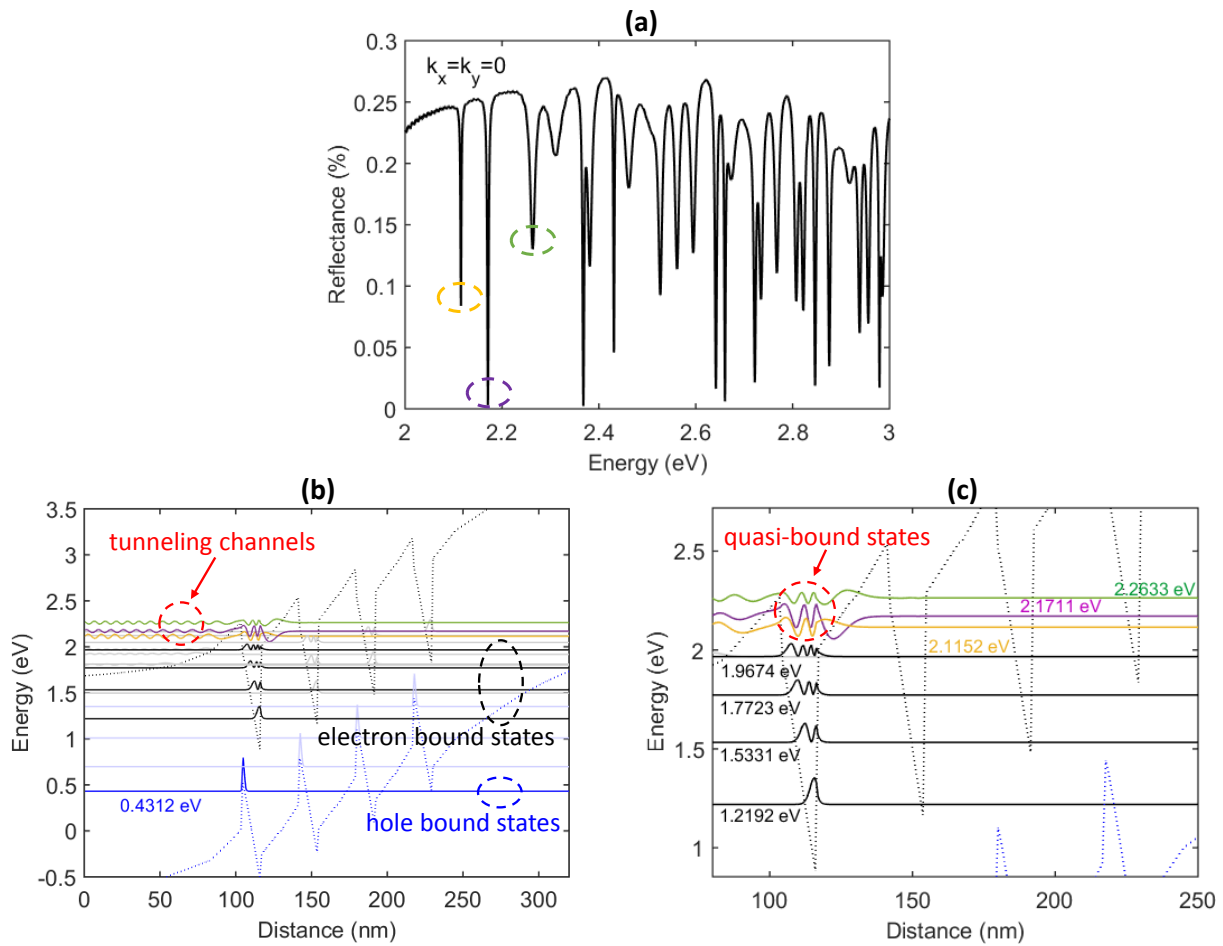


Figure 10: (a) Reflection spectra in the $\text{In}_{0.91}\text{Ga}_{0.08}\text{N}/\text{In}_{0.4}\text{Ga}_{0.6}\text{N}$ multi-QW structure for $k_x = k_y = 0$ obtained by TMM. (b) Low-lying quasi-bound and bound states in the multi-QW structure. (c) Enlarged view for the quasi-bound states and bound states in multi-QW region.

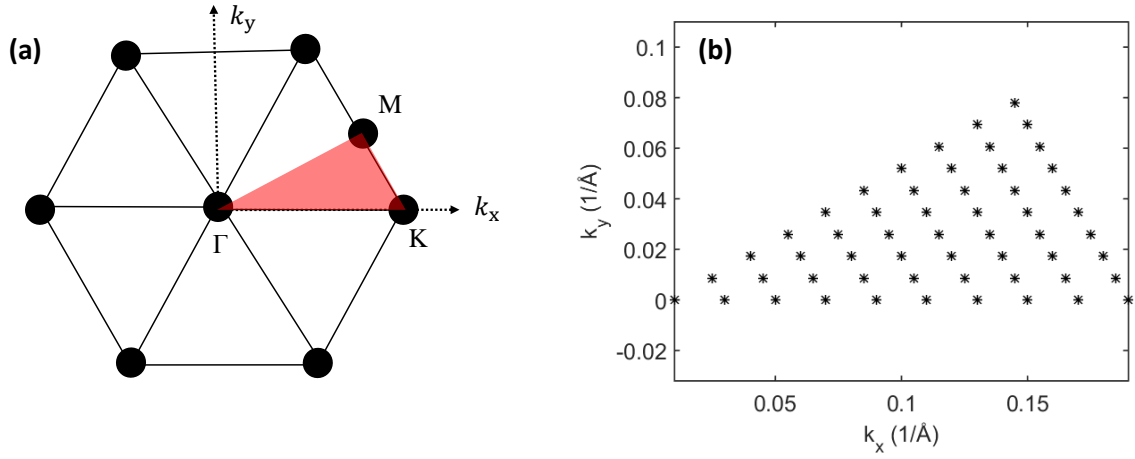


Figure 11: (a) Brillouin zone of a WZ quantum well. The grey area indicates the irreducible segment. (b) Sampling points of $\mathbf{k}_{||}$ in the irreducible segment used in the integration over $\mathbf{k}_{||}$.

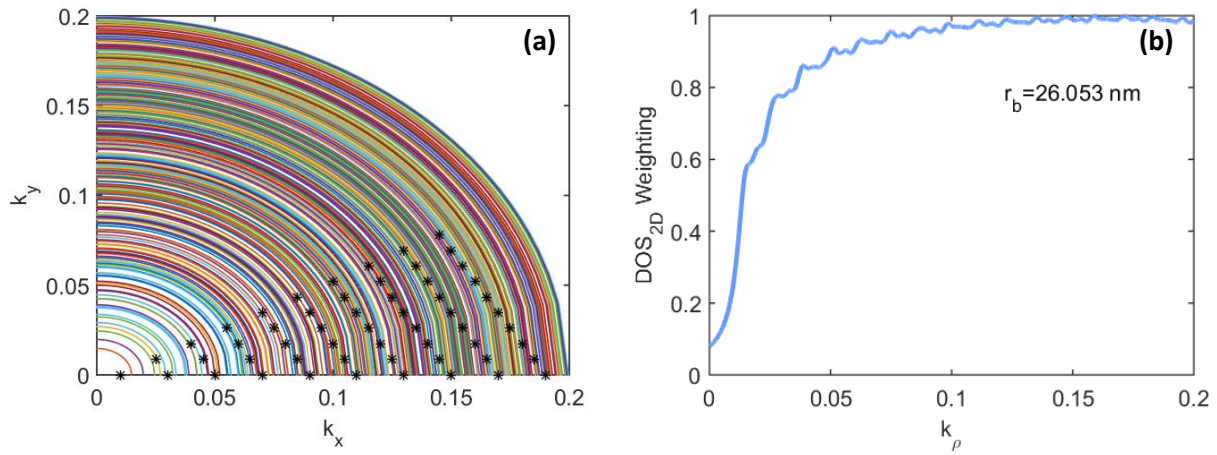


Figure 12: (a) Quantized states introduced by a cylindrical hard-wall boundary condition due to lateral confinement. (b) Density-of-states (broadened by a finite width) of laterally confined states for a cylinder of radius $r_0 = 26.053$ nm with infinitely high barrier.

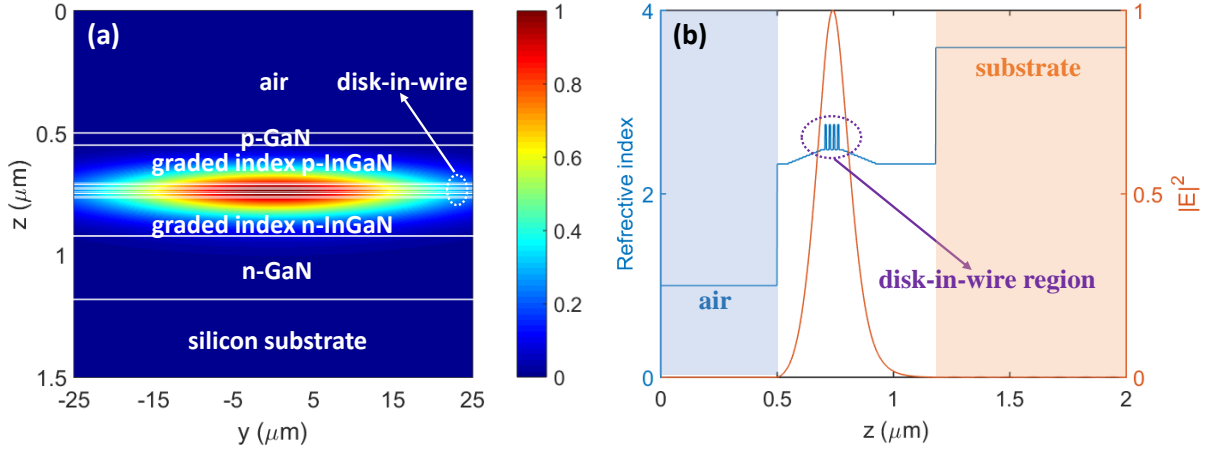


Figure 13: (a) Schematic diagram and the fundamental model profile of the InGaN disk-in-wire waveguide structure considered in the RCWA simulation. (b) Schematic diagram of spatial-dependent refractive index of the InGaN disk-in-wire waveguide structure.

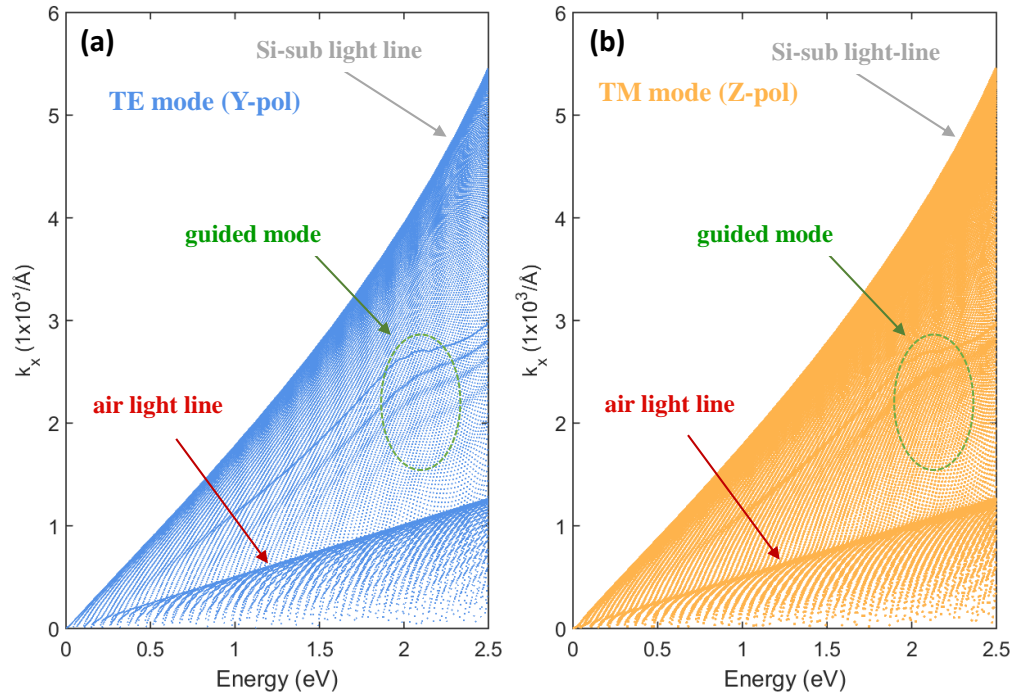


Figure 14: Photonic band structure of the $\text{In}_{0.91}\text{Ga}_{0.09}\text{N}/\text{In}_{0.4}\text{Ga}_{0.6}\text{N}$ graded-index waveguide structure for (a) TE mode component and (b) TM mode component.

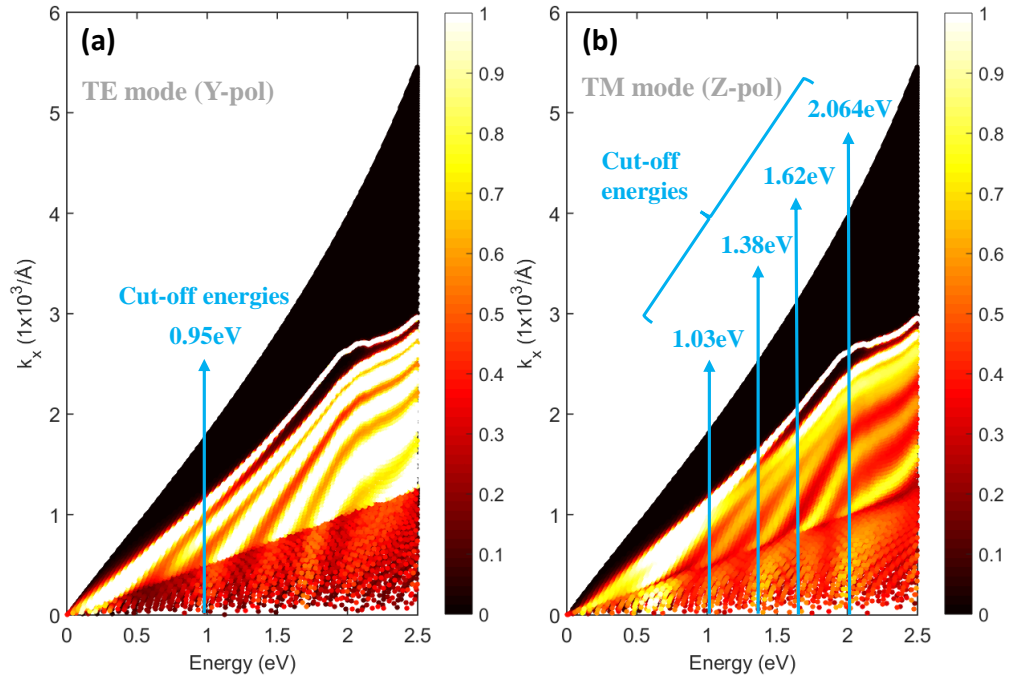


Figure 15: The normalized modal density in the nanowire layer of the $\text{In}_{0.91}\text{Ga}_{0.09}\text{N}/\text{In}_{0.4}\text{Ga}_{0.6}\text{N}$ graded-index waveguide structure for (a) TE and (b) TM polarization. The color bar indicates the probability strength of a mode in the nanowire layer

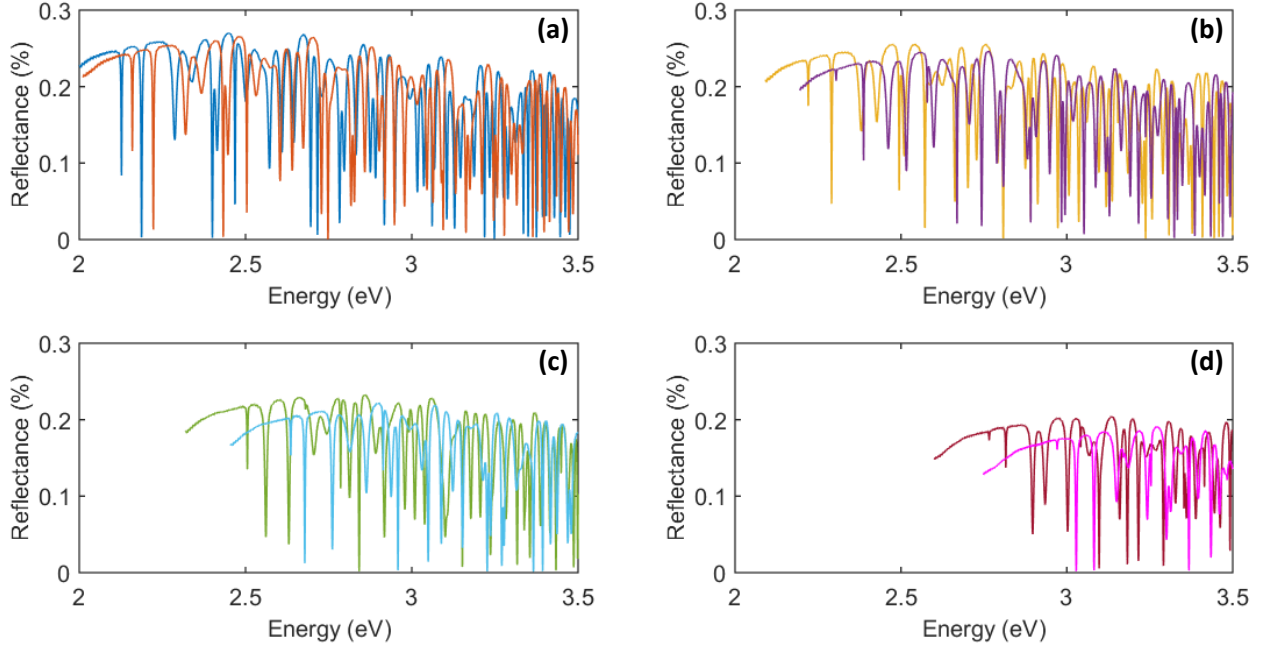


Figure 16: Individual contributions to the reflection spectra from various sampling points for \mathbf{k}_{\parallel} , calculated by TMM with EBOM. (a) $\mathbf{k}_{\parallel} = (0.0177, 0.0), (0.0443, 0.0154)$. (b) $\mathbf{k}_{\parallel} = (0.071, 0.031), (0.0975, 0.046)$. (c) $\mathbf{k}_{\parallel} = (0.124, 0.061), (0.151, 0.077)$. (d) $\mathbf{k}_{\parallel} = (0.177, 0.092), (0.204, 0.107)$.

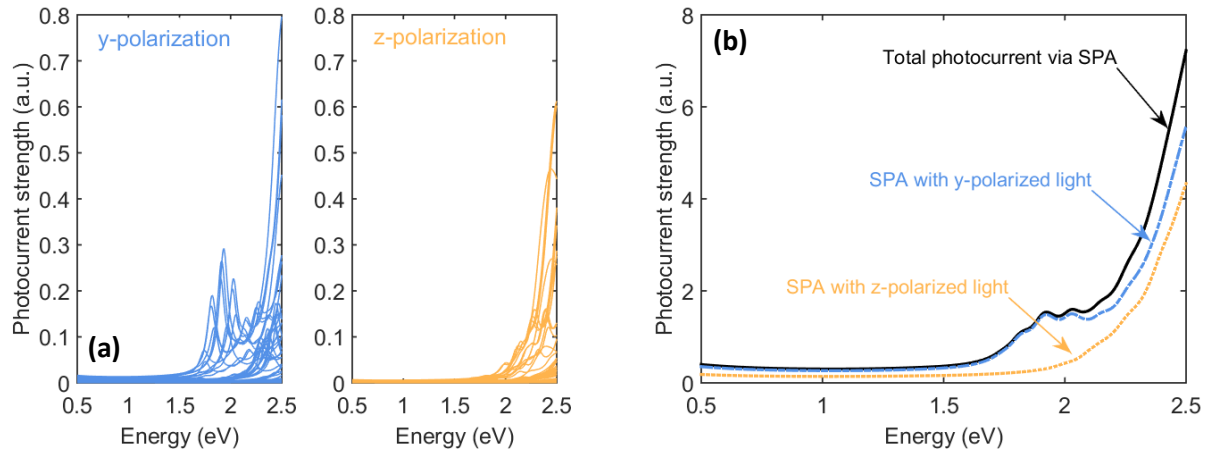


Figure 17: Photocurrent spectra via SPA process with both y-polarized and z-polarized light. (a) Individual contributions from various sampling points for \mathbf{k}_{\parallel} . (b) Total SPA photocurrent spectra.

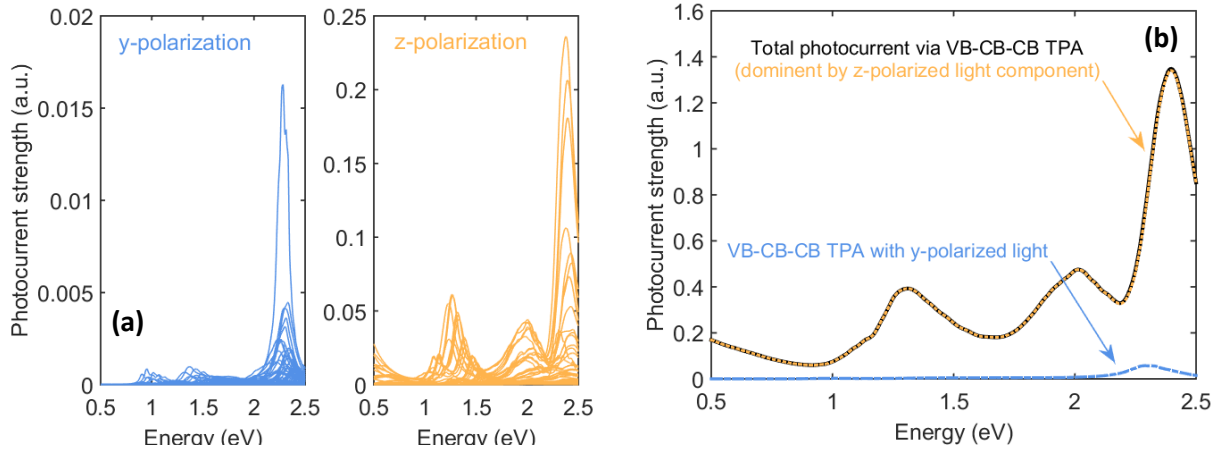


Figure 18: Photocurrent spectra via VB-CB-CB TPA process with both y-polarized and z-polarized light. (a) Individual contributions from various sampling points for \mathbf{k}_{\parallel} . (b) Total TPA photocurrent spectra from VB-CB-CB process.

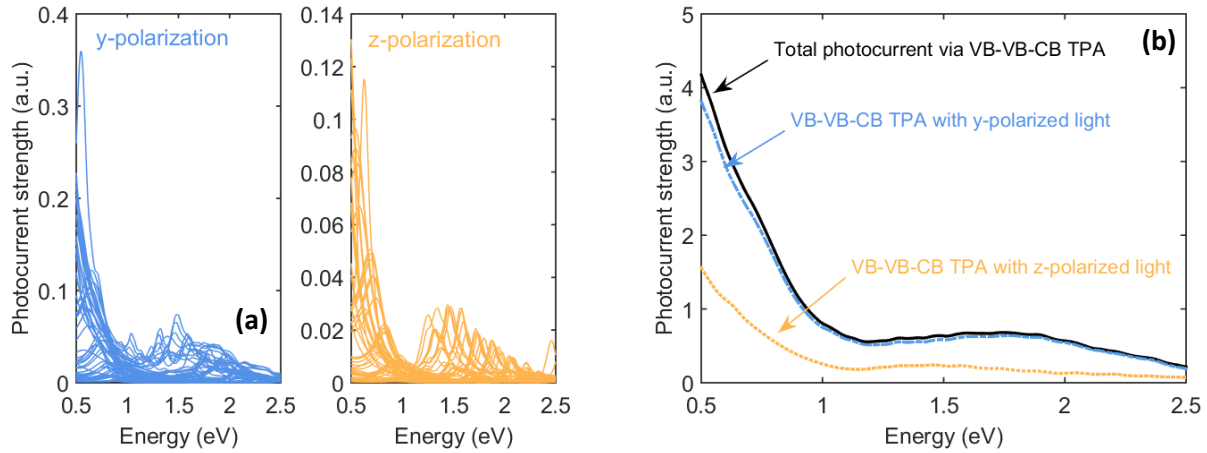


Figure 19: Photocurrent spectra via VB-VB-CB TPA process with y-polarized and z-polarized light. (a) Individual contributions from various sampling points for \mathbf{k}_{\parallel} . (b) Total TPA photocurrent spectra from VB-VB-CB process.

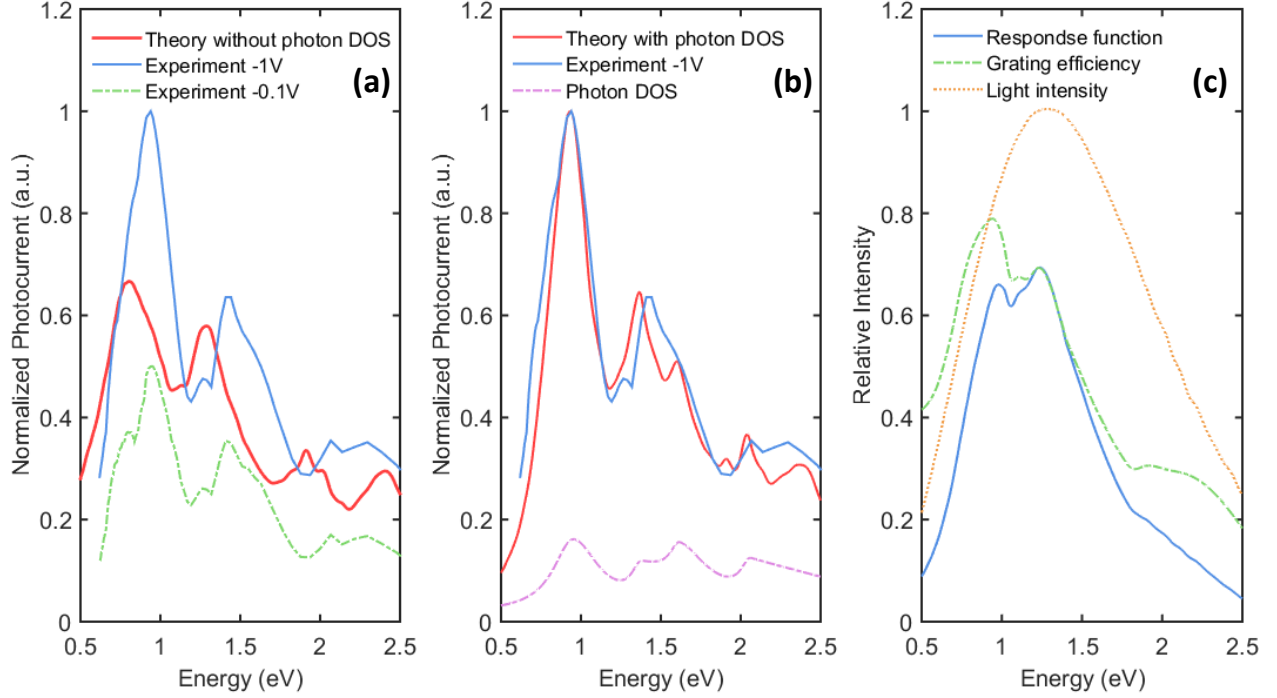


Figure 20: Calculated photocurrent spectra and the comparison with experimental data (a) without including effects due to photon DOS and (b) including effects due to photon DOS. (c) The equipment response functions and light intensity profile used in this work.

Conclusions

Comprehensive modeling of the photocurrent spectrum for an $\text{In}_{0.91}\text{Ga}_{0.09}\text{N}/\text{In}_{0.4}\text{Ga}_{0.6}\text{N}$ disk-in-wire guided wave photodiode operating from $1.3 \mu\text{m}$ to $1.55 \mu\text{m}$ has been demonstrated. The model contains strain effects, piezoelectric effects, and the effects of the photon DOS in the calculation. This model has been used to systematically study the electronic, optical, and transport properties in this $\text{In}_{0.91}\text{Ga}_{0.09}\text{N}/\text{In}_{0.4}\text{Ga}_{0.6}\text{N}$ disk-in-wire photodiode. Our model successfully predicts photocurrent spectra which agree fairly well with the experimental data. The physical mechanisms for the peaks observed in the experimental photocurrent spectrum are investigated. This is the first direct comparison between the comprehensive theoretical analysis for III-N disk-in-wire structure and the experimental data for the high-indium-content device. The presented approach can be easily applied in III-N materials system

with arbitrary complex nanostructures, in which the realistic band structure over the full BZ is incorporated efficiently. Besides that, the presented method utilizing the reflectance spectrum calculation in multi-band TMM method is especially suitable for the simulation of devices driven by optical pumping. It is expected this model can be utilized to study other aspects of III-N devices with ultra-high indium mole fraction.

Acknowledgement

This work is supported by the National Science Foundation (MRSEC program), under Grant DMR-1120923, and Ministry of Science and Technology (MOST), Taiwan under contract no. 109-2112-M-001-046.

References

- (1) A. W. Fang, H. Park, O. Cohen, R. Jones, M. J. Paniccia, and J. E. Bowers, *Opt. Express* **14**, 9203–9210 (2006).
- (2) D. Liang, and J. E. Bowers, *Nat. Photonics* **4**, 511–517 (2010).
- (3) S. Tanaka, S.-H. Jeong, S. Sekiguchi, T. Kurahashi, Y. Tanaka, and K. E. Morito, *Opt. Express* **14**, 9203–9210 (2006).
- (4) A. Y. Liu, C. Zhang, J. Norman, A. Snyder, D. Lubyshev, J. M. Fastenau, A. W. Liu, A. C. Gossard, and J. E. Bowers, *Appl. Phys. Lett.* **104**, 041104 (2014).
- (5) Z. Mi, P. Bhattacharya, J. Yang, and K.P. Pipe, *Electron. Lett.* **41**, 742–744 (2005).
- (6) H. Z. Chen, A. Ghaffari, H. Wang, H. Morkoc, and A. Yariv, *Appl. Phys. Lett.* **51**, 1320–1321 (1987).
- (7) S. Jahangir, T. Schimpke, M. Strassburg, K. A. Grossklaus, J. M. Millunchick, and P. Bhattacharya, *IEEE J. Quantum Electron.* **50**, 530–537 (2014).

- (8) S. Jahangir, M. Mandl, M. Strassburg, and P. Bhattacharya, *Appl. Phys. Lett.* **102**, 071101 (2013).
- (9) H. P. Trung Nguyen, K. Cui, S. Zhang, S. Fatholouloumi, and Z. Mi, *Nanotechnology* **22**, 445202 (2011).
- (10) W. Guo, M. Zhang, A. Banerjee, and P. Bhattacharya, *Nano Lett.* **10**, 3355–3359 (2010).
- (11) S. R. White, and L. J. Sham, *Phys. Rev. Lett.* **47**, 879 (1981).
- (12) B. A. Foreman, *Phys. Rev. B* **56**, R12748 (1997).
- (13) A. Hazari, F.-C. Hsiao, L. Yan, J. Heo, J. M. Millunchick, J. M. Dallesasse, and P. Bhattacharya, *Nano Lett. IEEE J. Quantum Electron.* **53**, 1–9 (2017).
- (14) Y. C. Chang, *Phys. Rev. B* **37**, 8215 (1988).
- (15) Y. C. Chang, and W. E. Mahmoud, *Comput. Phys. Commun.* **196**, 92 (2015).
- (16) F.-C. Hsiao, C. T. Liang, Y. C. Chang, and J. M. Dallesasse, *Comput. Phys. Commun.* **252**, 107139 (2020).
- (17) M. G. Moharam, E. B. Grann, D. A. Pommet, and T. K. Gaylord, *J. Opt. Soc. Am.* **12**, 1068–1076 (1995).
- (18) P. N. Keating, *Phys. Rev. B* **145**, 637 (1966).
- (19) R. Martin, *Phys. Rev. B* **1**, 4005 (1970).
- (20) H. Jiang, and J. Singh, *Phys. Rev. B* **56**, 4696 (1997).
- (21) D. Camacho, and Y.M. Niquet, *Physica E* **42**, 1361–1364 (2010).
- (22) M. Mitchell, *Symmetry and Strain Induced Effects in Semiconductors* (Wiley, Halsted, UK, 1974).

- (23) D. J. Chadi, and Marvin L. Cohen, Phys. Rev. B **8**, 5747 (1973).
- (24) E. J. Austin, and M. Jaros, Phys. Rev. B **31**, 5569 (1985).
- (25) D. Ahn, and S. L. Chung, Phys. Rev. B **34**, 9034 (1986).
- (26) V. A. Mandelshtam, T. R. Ravuri, and H. S. Taylor, Phys. Rev. Lett. **70**, 1932 (1993).
- (27) D. M. T. Kuo, and Y. C. Chang, Phys. Rev. B **61**, 11051 (2000).
- (28) D. Z.-Y. Ting, E. T. Yu, and T. C. McGill, Phys. Rev. B **45**, 3583 (1992).
- (29) J. N. Schulman, and Y. C. Chang, Phys. Rev. B **4**, 2346 (1983).
- (30) F. Bassani, and G. P. Parravicini, *Electronic States and Optical Transitions in Solids* (Pergamon, New York, 1975).
- (31) Y. C. Chang, J. Cheung, A. Chiou, and M. Khoshnevisan, J. Appl. Phys **68**, 4233 (1990).
- (32) V. I. Gavrilenko, and R.Q. Wu, Phys. Rev. B **61**, 2632 (2000).
- (33) S. L. Cunningham Phys. Rev. B **10**, 4988 (1974).
- (34) C. J. Chang-Hasnain, and W. Yang, Adv. Opt. Photonics **4**, 379–440 (2012).